MONASH University

Study of Mechanical and Electrical Properties of Engineered Cementitious Composites for Self-sensing Application

Leifeng Shi

Bachelor of Engineering (Honours)

A thesis submitted for the degree of *Doctor of Philosophy* at

Monash University in 2018

Faculty of Engineering

December, 2018

- Study of Mechanical and Electrical Properties of Engineered Cementitious Composites for Self-sensing Application-

Copyright notice

Abstract

Engineered cementitious composites (ECCs) is one kind of cement-based material containing a small volume fraction of randomly distributed short high-performance fibres, offering excellent mechanical properties and featuring a potentially proper self-sensing property enhanced by the filled functional fibres which demonstrate relatively high and stable conductivity. Current studies for self-sensing behaviour of ECC are limited for the lack of quantitative information of cracking damage and the technologies used are quite complex and expensive to be conducted. This study aims to observe and develop the self-sensing property of ECCs aided by some advanced technologies to provide a comprehensive understanding of conductivity property of ECCs and an effective way to optimise the design of ECCs. Literature review in terms of composition, material properties and failure mechanism of ECC was introduced. Electrical resistance measurement methods for cementitious materials were presented. The self-sensing study and electrical resistivity tomography (ERT) methods based on these measurement methods about ECC were reviewed. Some preliminary studies have been conducted for ECC fabrication, ECC resistance measurement and proposed technique review and validation.

The main content of this study contains three parts. The first study presents the prediction of mechanical and electrical properties of ECC based on the artificial neural network (ANN) technique with the aim of providing a gateway for a more efficient and effective approach in ECC design. Specifically, neural network models were developed for ECCs reinforced with polyvinyl alcohol (PVA) fibre or steel fibre (SF) with experimental data collected from other researchers for training. The development, training and validation of

the proposed models were discussed. To assess the capability of well-trained ANN models for property prediction, experimental studies were conducted, including compression test, four-point bending test, tensile test and electrical resistance measurement for ECCs of various composition. Excellent consistency between the predicted and tested results was obtained, demonstrating the feasibility of ANN models for property prediction of ECCs.

In the second study, mechanical and electrical properties of steel fibre-PVA ECC (SF-ECC) and carbon black-PVA ECC (CB-ECC) are investigated. Four-point bending and uniaxial tensile tests synchronising alternating current resistance measurement were implemented to obtain stress-strain relationships and electrical resistance, which were correlated with cracking development. In parallel, discrete element method (DEM) was applied to simulate the development of crack density during flexural and tensile testing. The outcomes for these two types of ECC were also compared to evaluate the sensitivity of self-sensing property for possible crack identification, which could contribute to the optimisation of ECCs with balance between mechanical and self-sensing capacities.

The third part of this study introduces a new ERT method for a SF- ECC based on its self-sensing property for crack identification. To study the feasibility and accuracy of the proposed method, specimens were prepared with different crack scenarios, namely a single edge crack, an additional crack in a specimen with an existing crack, a single diagonal internal crack, and dual edge cracks, followed by practical uniaxial tensile test, which were designed based on the most commonly occurring crack patterns. The resolution of the proposed method was also studied with various sizes of single edge cracks. The outcomes of this study can provide a simple but sound and convenient method for damage detection in structures containing ECC or other conductive cementitious materials.

Declaration

This thesis contains no materials which have been accepted for the award of any other degree or diploma at any university or equivalent institution and that, to the best of my knowledge and belief, this thesis contains no materials previously published or written by another person, except where due reference is made in the text of the thesis.

Signature: …….

Print Name: …Leifeng Shi……

Date: ……08/12/2018……

Acknowledgements

I would like to show my sincere appreciation to my main supervisor Dr. Ye Lu, who is never tired to share his experience, to provide patient guidance and give valuable advice for my life of research as a PhD candidature at Monash University. My work could not be successfully finished in time, without the ideas and suggestions from him. Thanks for the opportunities provided to me for attending the top conferences in my field, which helped me to broaden my horizon and acquired deeper understanding of my research topic as well as other innovative work being conducted by peers. Dr. Ye Lu also tried his best to offer me some part-time positions, such as tutor and research assistant, which really helped me a lot to concentrate on my research. I would also like to thank my co-supervisor Prof. Yu Bai, for his support and help to my studies.

I would like to thank all the staff at Civil Engineering Lab of Monash University, who gave me patient training and kind assistance to my experimental studies, especially Mr. Long Goh and Mr. Phillip Warnes.

Lastly, I would like to express my great gratefulness to my parents and my wife. Their support and love are my strongest power to face and enjoy the challenge during my PhD candidature.

Table of contents

Notations

The abbreviations commonly used in this thesis are listed below with corresponding definitions.

AC	Alternating current
ANN	Artificial neural network
CB	Carbon black
COD	Crack opening distance
DC	Direct current
DEM	Discrete element method
ECC	Engineered cementitious composite
EIT	Electrical impedance tomography
ERT	Electrical resistivity tomography
FEM	Finite element method
FRC	Fibre-reinforced concrete
GF	Gauge factor

HPFRCC	High performance fibre-reinforced cement composite
HRWR	High-range water reducer
PE	Polyethylene
PFC	Particle flow code
PP	Polypropylene
PVA	Polyvinyl alcohol
SF	Steel fibre
SFRC	Steel fibre-reinforced concrete

List of Figures

List of Tables

Chapter 1 Introduction

1.1 Self-sensing behaviour of cementitious materials

Concrete is one of the most used artificial construction materials in the world. It provides superior strength, durability and fire resistance, which makes the structures made of concrete can have a long service life. However, in current stage, due to the degeneration of material, impact by the service environment and lack of health monitoring, many concrete structures are in the state of utter disrepair. In particular, the undetected microcracks in cement-based material can extend and enlarge, leading to structural failure. This condition may cause catastrophic consequence if no inspection and maintenance are conducted in time. On June 2012, the parking roof collapsed at Algo Centre Mall in Canada. The metal and concrete debris crashed down through two floors of the shopping centre, killed 2 people and injured more than 20 people [1]. The main issue resulting this failure is because of no detection and monitoring of the defects on the roof. Similar accident happened on 14 August 2018, during a torrential rainstorm, a 210-metre section of Ponte Morandi collapsed [2] in Italy. The lack of maintenance and strengthening partially caused the collapse, which killed 43 people.

These disasters can be avoided if appropriate and effective monitoring and inspection would have been taken in time to the concrete structures. To monitor the health of civil infrastructure which is constructed with concrete, various crack detection techniques are widely applied based on different methodologies such as audio-visual, sonic/ultrasonic, electro-magnetic, deterministic, electric, infra-red thermography and radiography [3, 4].

The majority of these methods require the addition of built-in and/or surface-attached sensors, involving expensive and complex instrumental setups.

Self-sensing behaviour in concrete is an ideal solution to resolve this issue. With such a behaviour, it is possible to monitor stress, strain and damage by measuring electrical properties, including electrical resistance, dielectric constant and polarisation resistance, without the need for external sensor implementation [5, 6]. Since the self-sensing property originates from changes in the conductive network in the material, conductivity is the most representative feature of sensing behaviour and was studied by many researchers [6].

Engineered cementitious composite (ECC) is one kind of cement-based material containing a small volume fraction of randomly distributed short high-performance fibres up to 2% [7], featuring a potential self-sensing application enhanced by the filled functional fibres which demonstrate relatively high and stable conductivity. It is also a special class of high-performance fibre-reinforced cement composite (HPFRCC) offering excellent mechanical properties such as high tensile strength, large pseudo-strain-hardening capacity, and high energy absorption [8-10]. Therefore, this study will focus on the mechanical and electrical properties of ECC for self-sensing applications.

1.2 Motivation and objectives

The design for ECC can be based on the micromechanics related to the interaction between fibres and matrix. However, from the theoretical material design to practical application, it requires a complex process starting with microstructure tailoring and optimisation, followed by time-consuming experimental and finite element analyses [9]. For the intrinsic self-sensing properties of ECCs, most researchers are interested in the relationship between

the fractional changes in resistivity $\Delta\rho/\rho_0$ and strain change or cracking development during the load test. Also, many parameters were used to assess self-sensing properties, such as input/output range, linearity, repeatability, hysteresis, signal-to-noise ratio and zero shifts [11]. In particular, ECCs enhanced by steel fibre (SF) or carbon black (CB), which demonstrate relatively high and stable electrical conductivity, show superior sensitivity to crack development in quantity and quality [12-14]. However, despite the studies of damage detection in SF- and CB-ECC, there was little investigation of the different characteristics of these two conductive fillers in relation to cracking development. Such a study could provide a fundamental understanding for designing excellent self-sensing ECCs for crack identification along with good mechanical performance.

The microcracks in cement-based material may extend and enlarge and lead to visible macrocracks, implying that the density of microcracks can partly reflect the loading condition. Previous studies showed some relationship between the conductivity of ECCs and stress, strain and crack density [6, 15]. However, these studies were limited for the lack of quantitative information of cracking damage. The electrical resistivity tomography (ERT), which can construct the conductivity image for the object, is proposed in this study to provide a comprehensive understanding of conductivity property of ECCs. To construct the ERT, the common method is based on a complete electrode model [16-18] to insert a regulate AC into a pair of electrode and measure the voltages for the rest pairs. Then the finite element method (FEM) model is meshed and the resistivity for each point is obtained by solving the forward and inverse problems. The existing ERT approaches applied to cement-based material, although they can localise damage and trace crack development,

are complex and require numerous measurements for high-resolution images. In this research, the specific objectives are as follows:

- To optimise the design of ECCs and improve self-sensing and mechanical properties by artificial neural network (ANN) technique.
- To establish a quantitative relationship between electrical resistance and micro-cracking density in various loading tests, e.g. uniaxial tensile test and four-point bending test.
- To verify the feasibility and accuracy of a probabilistic diagnostic algorithm for ERT construction, so as to characterise the damage development in ECCs.
- To study the feasibility of the proposed ERT method for monitoring crack propagation in practical application.

1.3 Thesis outline

Chapter 1 introduces the background, motivation and objectives of the study and the contents of following chapters, which indicates the research gap and aims of this study.

Chapter 2 reviews the composition and relevant material properties of ECC, to get a better knowledge about ECC. The design theory and mechanism are also introduced to understand the characteristics of ECC other than normal concrete.

Chapter 3 provides a fundamental understanding for self-sensing study. Electrical resistance measurement methods for cementitious materials are reviewed. Some previous

studies about self-sensing behaviour of ECC are introduced. The principles and methodology of ERT are introduced. The application of ERT for ECC is reviewed.

Chapter 4 introduces the experiment preparation process for all the following studies, such as ECC specimen fabrication and electrical measurement method selection. Some novel techniques which will be applied for the studies in the next chapters, such as DEM, ANN and ERT are introduced and reviewed in detail. Some preliminary work for methods or technique validation are also presented.

Chapter 5 shows the development of several ANN models correspondingly in order to predict the electrical and mechanical properties, such as resistivity, compressive strength, flexural strength and tensile strength, of some typical ECCs fabricated with PVA and SF. The datasets for ANN training are based on a comprehensive literature review of previous studies. A set of experiments including compression test, four-point bending test, tensile test and electrical resistance measurement for ECCs with various proportions of PVA and SF were conducted to demonstrate the capability of ANN models in predicting the mechanical and electrical properties of ECCs.

Chapter 6 provides a fundamental understanding for designing excellent self-sensing ECCs for crack identification along with good mechanical performance. Experiments using the four-point bending test and uniaxial tensile testing synchronised with electrical resistance measurement were conducted for SF-ECC and CB-ECC specimens to explore the stress-strain relationship and conductivity performance in each test. DEM models were created to simulate crack density development during the tests. The self-sensing capacities related

to crack development in each type of ECC are discussed and compared on the basis of the results of experiments and simulations.

Chapter 7 introduces a probabilistic diagnostic algorithm to detect cracking in ECC with the involvement of fewer measurements and simpler tomography reconstruction than normal ERT method. The feasibility and accuracy of this method were studied using SF-PVA ECC specimens with a single edge crack, an additional crack in a specimen with existing crack, a single diagonal internal crack, and dual edge cracks, followed by uniaxial tensile tests, representing the most frequently occurring crack patterns.

Chapter 8 presents the conclusions of the thesis and recommendations for future work.

Chapter 2 Engineered cementitious composites: material property and failure mechanism

The chapter reviews the composition and relevant material properties of ECC, to get a better knowledge about the characteristics of ECC. The failure mechanism is also introduced to understand the principles of the superiority of ECC than other normal concrete.

2.1 Composition and material properties of ECC

Cementitious materials are widely used in construction of many key engineered structures. However, cement-based concrete, which is a quasi-brittle material, has an inherent weakness in resisting tensile stress, and is inclined to exhibit extensive cracking and suffer brittle failure, with low shatter resistance under impact loading. In this respect, steel rebar-reinforced or prestressed concrete has been widely used in engineered structures since the 19th century, which are usually constructed with bulk wall thickness to resist tension, impact and blasts. On the other hand, fibre-reinforced concrete (FRC) is composed of cement, water, sand, fly ash and some chemical additives, with a moderate volume fraction of randomly distributed short fibres, without much variation in the processing and fabrication procedures of conventional cement-based concrete. It is considered to be a good substitute for conventional concrete materials in protective structures due to its high resistance to shatter with reduced scabbing, spalling, fragmentation and damage zone, and its increased energy absorption due to distributed microcracking [9, 19]. High strength steel fibre-reinforced concrete (SFRC) is now used extensively as a construction material as it

has been proven to be highly effective in resisting impact loading [20]. An ECC is a special class of high-performance fibre-reinforced cement composite (HPFRCC), which usually has a total fibre volume fraction of less than or equal to 2%, and is reinforced with short high performance fibres such as SF, polypropylene (PP), polyethylene (PE) and polyvinyl alcohol (PVA) fibres. It offers significantly improved mechanical properties over regular FRCs [8] and is a promising engineering material for protective structures due to its excellent mechanical properties such as high tensile strength, large pseudo-strain-hardening capacity to resist microcracking, and high energy absorption [10, 21]. The significant low fibre content in ECCs compared to regular FRCs reduces not only the material cost but also the intensive labour cost incurred with the fabrication of FRCs.

The type, geometry and volume fraction of fibres play important roles in tailoring the mechanical behaviours of an ECC [21, 22]. A hybrid fibre-reinforced ECC, with a proper volume of both high modulus fibres such as SF and low modulus fibres such as PVA or PE, is expected to improve both tensile strength and strain capacity, which are important for energy absorption [23] and impact resistance. A study of the mechanical behaviour of an ECC reinforced with both SF and PE fibres [24] demonstrated that it exhibits better tensile strength than that reinforced with only PE fibres, and greater tensile strain capacity than that reinforced with only SF fibres. Experimental studies of the high-velocity impact behaviour of ECCs demonstrated the great potential of hybrid FRC structures to resist impact, with improved shutter resistance and reduced scabbing, spalling, fragmentation and extent of damage [23, 25].

Apart from excellent mechanical properties, ECC made by some functional fillers also provide proper self-sensing behaviour. In particular, ECCs enhanced by SF or carbon black

(CB), which demonstrate relatively high and stable electrical conductivity, have shown superior sensitivity to crack development in quantity and quality [12-14]. As low resistive materials, both SF and CB can be considered pure conductors. They can improve the conductivity of cement matrix by forming unimpeded conductive pathways. Particular proportions of these two materials have been recommended for obtaining the best general conductive capacity of ECCs [13, 14, 26], but a greater mixture of fibres would not yield any improvement as there is an electrical percolation threshold [27]. If the filler content exceeds that threshold, neither conductivity nor mechanical properties would be effectively increased. The effects of combinations of SF and CB in ECC have also been studied [28]. A linear relationship between the fractional changes in surface impedance of ECC beams and the crack opening distance (COD) at mid-span has been found under the three-point bending test.

2.2 Failure mechanism

The failure mechanism of ECC is based on micromechanics and fracture mechanics. As shown in Figure 2.1, there are three types of tensile failure modes for cementitious materials: brittle, quasi-brittle and strain-hardening failure [29].

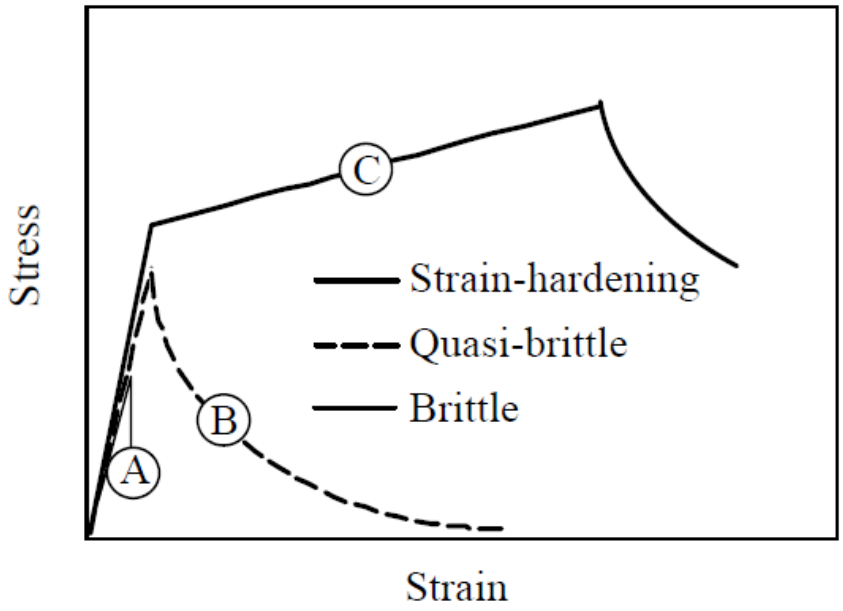

Figure 2.1 Three types of failure modes observed in cementitious materials [29].

Brittle failure mode usually occurs in hardened cement paste materials. The typical characteristic is reflected by the stress-strain curve as an increasing linear curve followed by a dramatical drop, when the first cracking come up. The ultimate tensile strain is less than 0.01%. Quasi-brittle failure is characterised by a linear stress-strain curve with a gradual decreasing trend after the first cracking. This failure is happened for the bridging effect of the aggregates or other add-in functional fillers. Once the material is defined with good strain-hardening behaviour, it can resist more load after the initial cracking happened. The stress-strain curve keeps growing up at a lower rate while the material is still suffering larger deformation after multiple cracking generated [30].

ECC is of great strain-hardening behaviour due to the bridging mechanism of the short fibres. The fibre-bridging model was proposed for short fibre reinforced cementitious material [31, 32]. For instance, the single fibre pullout behaviour is shown in Figure 2.2

for a type of PVA-ECC [33]. As the applied load increases, the bond between the fibre and surrounding cement matrix breaks up firstly, that causes the first contemporary drop of the load. After that, the fibre is in pullout stage and slips away from the cement matrix. The frictional force will increase and shows a slip-hardening behaviour of the fibre. Such a phenomenon of all the internal fibres in the ECC cement matrix will enable ECC to carry increasing load after first cracking and show ideal strain-hardening behaviour. Based on that pseudo strain-hardening model of ECC was put forward and modified to show the strain hardening behaviour and the multiple cracking [34, 35].

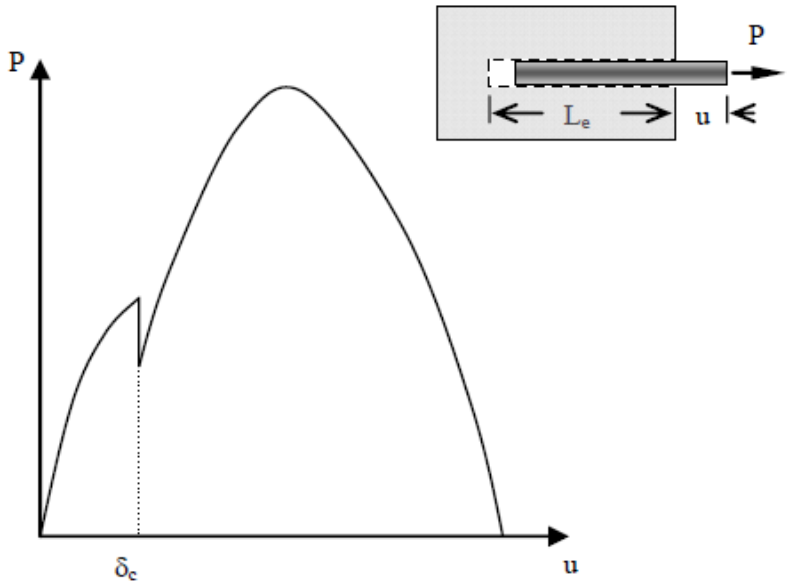

Figure 2.2 Single fiber pullout behaviour of the PVA fibre [33].

There are two criteria for the strain-hardening behaviour of ECC. The first one is the strength criterion, which determine the initial cracks [36] as

$$\sigma_{fc} \leq \sigma_0 \,, \tag{2.1}$$

where σ_{fc} is the first cracking strength; σ_0 is the maximum fibre-bridging capacity on each potential crack plane. If the fibres have been pulled out or ruptured, the initial cracking section will lose tensile capacity.

The other important criterion for the multiple cracking behaviour, which can transit the failure mode of ECC from quasi-brittle to strain-hardening, is steady state cracking criterion [31, 32, 34, 37]. When the initial cement matrix crack is generated, the short fibres can hold and connect the cracking interfaces. With the opening of the crack, the bridging stress is increasing and may reach the magnitude of the applied load to the ECC. Then the crack flanks flatten to maintain the constant stress level, which is so called steady state cracking stress [38]. In this state, the crack will extend with existing constant load, and will not be influenced by the tensile load. According to the J- integral analysis of a steady state crack, the energy balance is shown as

$$J_{tip} = \sigma_{ss}\delta_{ss} - \int_0^{\delta_{ss}} \sigma(\delta)d\delta \ , \tag{2.2}$$

where J_{tip} is the crack tip toughness, which can be approximated as the cementitious matrix toughness, since the fibre volume fraction of most fibre reinforced cementitious composites is less than 5%; σ_{ss} is the steady state stress; δ_{ss} expresses the flattened crack opening. The steady state stress should be less than the maximum bridging stress as $\sigma_{ss} \leq \sigma_0$ (2.3)

These two equations imply that the crack tip toughness J_{tip} should be lower or equal the complementary energy J_b' (Figure 2.3) [39] as

$$J_{tip} \leq J_b' = \sigma_0 \delta_0 - \int_0^{\delta_0} \sigma(\delta) d\delta. \tag{2.4}$$

Both parts of the Eq. (2.4) have been arranged, so that the left-hand part and the right-hand part of the inequality related to cementitious matrix properties and the fibers with interface properties respectively. Therefore, the equation contributes to the design of ECC fabricated in terms of selection of materials and tailoring method.

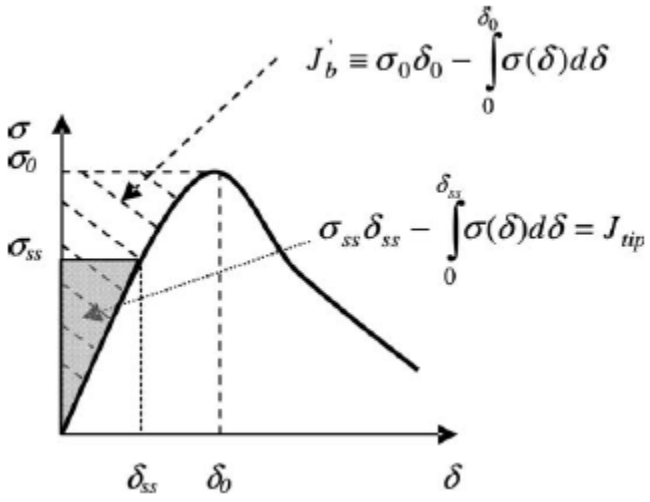

Figure 2.3 Relationship of fibre bridging stress and crack opening width [39].

2.3 Summary

In this chapter, the development of ECC is introduced. The characteristics of ECC are studied by reviewing different types of ECC with various material composition. The deeper understanding of failure mechanism of ECC will help the studies in the following chapters refers to design and optimisation of ECC properties.

Chapter 3 Self-sensing studies for cementitious materials

Electrical resistance measurement methods for cementitious materials are reviewed in this chapter to provide a basic understanding for self-sensing study. Some previous studies about self-sensing behaviour of ECC were introduced, to get the common research scopes relevant to self-sensing ECC. The principles and methodology of ERT were introduced. And the application of ERT for ECC was reviewed.

3.1 Measurement of electrical resistance

The self-sensing property refers to monitoring the stress, strain, crack and damage by measuring the electrical properties, including electrical resistance, dielectric constant and polarization resistance [5, 6], in which the electrical resistance or resistivity are the most commonly used indicator for assessing self-sensing behaviour for cement based materials [6]. Cement, the material itself, is of low conductivity, which can be regarded as an insulating material. Similar to the normal concrete, the conductivity of ECC mainly owe to the ions carried by pore water or solution. Moreover, the added-in high conductive functional fillers, like steel fibres (10^7 S/m) or carbon fibres (10^4 S/m) can form a frame of conductive paths, that can improve the intrinsic conductivity of ECC, even be developed as a class of electrical semi-conductive materials with electric conductivity of $10^2 – 10^8$ S/m. Although this kind of measurement of electrical resistance of ECC seems to be simple, there are many factors that can influence the measurement result, specifically, such as the concentration and geometry of fillers, cement-water ratio of concrete, moisture content,

temperature, humidity, electrode types etc. [40-44]. Therefore, these factors should be under well control while reliable and repeatable methods need to be put forward for the electrical resistance measurement.

3.1.1 Two-probe method and four-probe method

There are multiple measurement methods applied for cement-based materials for experiments in situ. Generally, in terms of electrode layout, two main categories based on electrical probe layout are widely used, which are so called two-probe method and four-probe method. As shown in Figure 3.1(a), two-probe method is the simplest way to get the average bulk resistivity for the whole specimen. For a non-destructive measurement, usually two metallic electrodes are attached to the two longitudinal ends of the specimen by conductive pastes or gels. Then these electrodes are connected to a current source and a voltage meter to form a circuit. Both DC and AC can be inserted, and the resistivity of the specimen can be obtained as

$$\rho = \frac{V}{I}\frac{A}{L}, \tag{3.1}$$

where V and I are the measured voltage and insert current. A and L represent the cross-section area and length of the specimen, respectively. Normally two-point method has a major issue that the contact impedance induced at the interface between the cement and electrodes will lead to a larger result for measurement. This is due to the electrical chemical reaction around that interface, which can produce an effective “back electromagnetic field” [45]. To overcome this drawback, four-probe method was more appreciated in field application as shown in Figure 3.1(b). The outer two electrodes are connected with a

constant current source and the inner two electrodes are used to measure the voltage jump in the certain distance. By using this method, the contact impedance will not be covered in the measured range and a relatively accurate measurement can be accomplished.

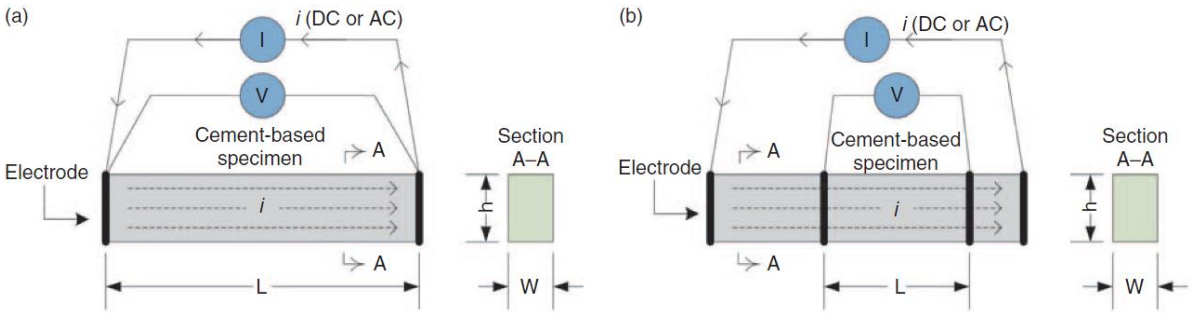

Figure 3.1 Conductivity measurement method: (a) two probe method; (b) four probe method [18].

3.1.2 Direct current (DC) and alternating current (AC)

Since the conductivity of cement is achieved by the charges stored in the pore water, cement also has capacitive properties. Thus, when a continuous DC is applied, an electrical polarisation phenomenon will be introduced. To be more specific, the positive and negative ions are separated by the mono-direction electrical potential, so that less current can pass through the conductive path way [45]. Then the measurement result of resistance will keep increasing after a fairly short duration, which will require a quick data record to minimise the impact of polarisation. McCarter and Brousseau [46] have put forward an AC measurement method with an equivalent circuit model for cement paste, by which the cement will be regarded as a parallel circuit of a resistor and capacitor (Figure 3.2). In this method, the high frequency AC will avoid the polarisation of ions and the result will include both resistance and capacitance, which is actually reflected as the amplitude of

impedance relevant to the frequency range. For frequency range 1 Hz-10 kHz, the phase angle of impedance is nearly 0°. Then the impedance measurement will display purely resistive behaviour [47]. It can be used for resistance measurement, without impedance analysis within a proper frequency range of AC.

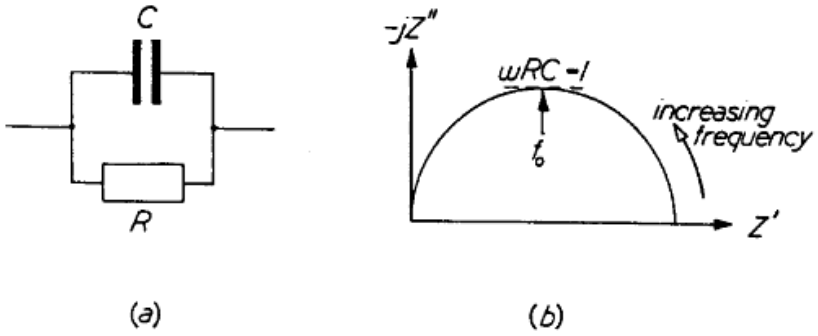

Figure 3.2 (a) Parallel electrical model and (b) impedance plotted in the complex plane [46].

3.1.3 Electrical percolation

An electrical percolation phenomenon was observed for cement composites containing conductive fibres [27]. The conductivity of ECC is not linearly related to the volumetric fraction of add-in fillers. There is s percolation threshold for different fibres, which is the most optimised volumetric fraction for electrical property design. As shown in Figure 3.3, the electrical resistivity is not influenced a lot in zone A when the filler concentration is fairly low. The conductive particles or fibres are not so well connected between each other, so that the conductive path ways are not built to allow the charges pass through the whole material. As the concentration keeps increasing, the resistivity of the composite deducts rapidly. Once the percolation threshold is reached, the acceleration of change in resistivity slows down. Finally, in zone C, the resistive capacity of composite keeps stable with more

fillers are used. In this stage, the conductive frame formed by the fillers already exists, the extra fillers are not able to form more effective conductive path. In addition, large quantities of add in fillers are facing to the difficulty of homogenous dispersion. The particles or fibres tend to form several large clumps, which may even result in failure of casting the ECC.

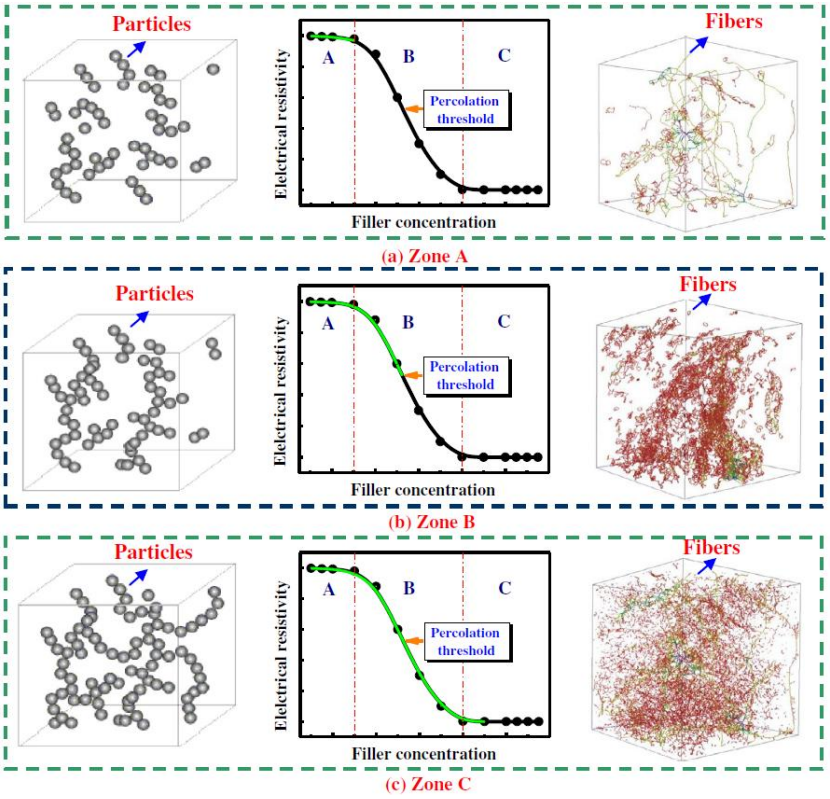

Figure 3.3 Change of the electrical resistivity along with filler concentration [6].

3.2 Self-sensing studies of ECC

The self-sensing property of ECC usually refers to using the resistive behaviour to monitor the structure deformation or defects. Since ECC is a type of HPFRCC, the sensitivity to electrical signal is enhanced by the randomly distributed and oriented filled-in fibres,

especially some of superior conductivity like SF and carbon fibre (CF) [42, 48, 49]. Therefore, this kind of cement-based materials shows great potential for non-destructive testing and structural health monitoring application.

Most researchers were interested in the relationship between the fractional changes in resistivity $\Delta\rho/\rho_0$ and strain change or cracking development during the load test. There are also many parameters to assess the sensing properties like input/output range, linearity, repeatability, hysteresis, signal to noise ratio and zero shifts [11]. For strain change monitoring, the gauge factor (GF) is defined in Eq. (3.2) as the fractional changes in electrical resistivity per unit strain [12, 15] to characterise the piezo-resistivity of ECC

$$GF = \frac{\Delta\rho/\rho_0}{\Delta\varepsilon}, \tag{3.2}$$

where $\Delta\rho$ is the resistivity change; ρ_0 is the original resistivity; $\Delta\varepsilon$ illustrates the strain change.

Various load tests were conducted for FRC to study self-sensing properties [6], while for ECC the uniaxial tensile test and bending test attracted more interests due to the good strain hardening and tensile strength of ECC. According to previous studies [48, 49] , the fractional changes in resistivity can reflect the progress of strain change and different loading stages relevant to different gauge factors, which is quite stable in their range. However, these studies omitted the influence by the cracking of ECC [12, 15, 28]. In this respect, Nguyen and co-workers [12] found that the reduction in electrical resistivity of SF reinforced concrete was strongly correlated with the increase in the numbers of micro-cracks in the strain-hardening stage. Ranade et al. [15] studied the crack patterns and used

the analytical method to predict the relationship between the single-crack behaviour (change in resistance across a unit area) and crack width. Ding et al. [28] found a linear relationship between the fractional changes in surface impedance of ECC beam under three point bending test and the COD of the macrocrack in the mid span. Unfortunately, previous studies still have not covered the influence of microcracking to the sensitivity of conductive capacity of ECC, which is relevant to the inherent mechanism of ECC and would contribute to the design of ECC.

3.3 Electrical resistivity tomography (ERT) of ECC

For quantitative study of the density of microcracking and the resistive capacity of ECCs, an imaging technique known as electrical impedance tomography (EIT) is introduced. With this method, it is possible to reconstruct the image of conductivity or permittivity of a measured object, a feature which has already been widely applied for damage detection and monitoring in geophysical exploration [50] and biomedical applications [51]. The basic procedure for EIT can be described in three steps. First, a series of electrodes are placed on the object in a proper layout. Constant current is injected into each pair of electrodes, while a voltage measurement is conducted for all the remaining pairs to acquire the boundary conditions. Then, a forward model, referred to as a complete electrode model [16], is simulated based on the measured boundary condition, with the unknown distribution of conductivity. Finally, the inverse problem can be solved by assuming various conductivity distributions until good convergence with the forward model is achieved [18]. ERT is a special case of EIT in which the capacitance is neglected. For the aforementioned cement-

based materials, a proper frequency range of the injected current will lead to the impedance being equal to the resistance, at which time a simpler ERT can be applied to the ECC.

3.3.1 Forward model

The most commonly used model for ERT is introduced by Cheng et al [16] as a complete electrode model, which can obtain the fundamental Poisson equation for ERT as

$$\nabla \cdot (\sigma \nabla u) = 0 \,, \tag{3.3}$$

where σ is electrical conductivity; u is electrical potential in the body. The equation is ruled by several boundary conditions. The first one is Dirichlet boundary condition, which can determine the electric potential of the lth electrode on the boundary as

$$U_l = u + z_l \boldsymbol{\sigma} \frac{\partial u}{\partial \boldsymbol{n}} \,, \tag{3.4}$$

where z_l is the contact impedance; $\boldsymbol{\sigma}$ is the distribution of conductivity in the body; $\boldsymbol{n}$ is the outward unit normal to boundary. The electric potential of each electrode would be impact by the contact impedance. The second boundary condition is Neumann boundary condition, which can determine the current density in the body. The lth electrode current equals to the integral of the current density through it as

$$I_l = \int_{e_l} \boldsymbol{\sigma} \frac{\partial u}{\partial \boldsymbol{n}} d\boldsymbol{S} \,, \tag{3.5}$$

where e_l is the electric potential under the electrode, and would equal to U_l when the contact impedance is zero. There is no current through the boundary as

$$\boldsymbol{\sigma}\frac{\partial u}{\partial \boldsymbol{n}} = 0\,. \tag{3.6}$$

Additionally, due to the charge conservation and the relation of ground and reference level of potential, the following equations need to be applied as

$$\sum_{\boldsymbol{l=1}}^{\boldsymbol{L}} \boldsymbol{I_l} = 0\,, \tag{3.7}$$

$$\sum_{\boldsymbol{l=1}}^{\boldsymbol{L}} \boldsymbol{U_l} = 0\,, \tag{3.8}$$

where L is the total number of the electrodes.

Based on the above equations, the complete electrode model can be numerically simulated by using FEM.

3.3.2 Image reconstruction

Based on the forward model, the boundary voltage of the objective can be obtained by giving the conductivity distribution, contact impedance and electrode current, which is a so-called well-posed problem. In ERT application, the boundary voltage can be measured, by which the conductivity distribution is supposed to be obtained. This inverse problem is so-called ill-posed problem, for which there are diverse solutions with high sensitivity to the modelling errors and measurement noise. One solution to the inverse problem of image reconstruction is provided by [18]. It requires to run the forward model repeatedly. To minimise the mean square error between the measured voltages and the predicted electric potential, the distribution of conductivity is varied

$$f(\sigma') = \frac{1}{2}\|u(\sigma') - U\|^2 , \tag{3.9}$$

where $\sigma' = \sigma + \Delta\sigma$; $\Delta\sigma$ is the changes in conductivity between successive run of the forward problem, which is based on Newton-Raphson iterative method and can be expressed as

$$\Delta\sigma = -[u'(\sigma)^T u'(\sigma)]^{-1} u'(\sigma)[u(\sigma) - U] , \tag{3.10}$$

where $u'(\sigma)$ is the Jacobian matrix of the FEM boundary potential, which is the voltage changes at the electrodes induced by small perturbations in the assumed conductivity distribution. Then Tikhonov regularisation method, one of the most commonly used regularisation method, can be used to reach the convergence to the final conductivity distribution [52].

3.3.3 ERT application for ECC

The first study of ERT for ECC was conducted by Hou and Lynch [18], who used a monotonic tensile test, a cyclic axial loading test and a three-point bending test of PVA reinforced ECC, as well as the ERT measurement. Optical images of each specimen at different loading stages were recorded and compared with the ERT mapping. The crack patterns showed great consistency and the feasibility of ERT for concrete application was verified. Karhunen and co-workers used another reconstruction method to solve the inverse problem [17, 53, 54]. Unlike early studies, a reference conductivity measurement and mapping prior to the loading test were no longer required to remove the inhomogeneity of the result. Based on the same theoretical principles, the concept of sensing skin was proposed, which is a thin layer of silver-based conductive paint applied on cement-based

materials [55, 56]. That concept shows great potential for practical applications of this kind of technique for concrete structures.

3.4 Summary

In this chapter, the electrical resistance measurement methods for cementitious materials were introduced and compared, which provides firm basis for resistance measurement method test and selection in Chapter 4. The self-sensing studies of ECC were reviewed and summarised. It is noticed that previous studies still have not covered the influence of microcracking to the sensitivity of conductive capacity of ECC, which is relevant to the inherent mechanism of ECC and would contribute to the design of ECC. Commonly used ERT methods and studies relevant to cementitious materials are illustrated, which provides a comprehensive understanding of ERT.

Chapter 4 Experiments preparation and technique application in ECC studies

This chapter introduces the experiment preparation for all the following studies, such as ECC fabrication and electrical measurement method selection. Some useful techniques which will be applied for the studies in the next chapters, such as DEM, ANN and ERT are shown and explained in detail. Some preliminary work for verifying the methods or techniques are also presented.

4.1 Experiment preparation

4.1.1 Material selection

The ECC material developed in this study refers to the design of the M45 type of ECC [7], a PVA fibre based cementitious material with superior ductility and tensile resistance. SFs and CB particles were utilised as functional fillers to improve the conductivity of the mortar and enhance the self-sensing capacity. The cementitious material was normal Portland cement with ASTM class F fly ash which was added as dispersion material to distribute the functional fillers and orient them randomly to prevent entanglement and close packing, improving the mixture's workability and material sustainability. However, the addition of fly ash can lead to slower strength development at an early age. To ensure overall optimal performance, the fly ash to cement ratio was set at 1.2 [8].

The SF-ECC was fabricated with 0.58% volume fraction of coppered micro-steel fibres WSF0213 and 1.75% volume fraction of PVA, which was REC 15×12 from Kuraray Co.,

Ltd. The steel fibres were 8 mm long and 200 μm in diameter, with tensile strength 2600 MPa. The PVA fibre was 12 mm long and 39 μm in diameter and was oil coated to reduce the bond strength between the fibre-matrix interfaces in order to facilitate the pull-out mechanism for the strain-hardening property. High-range water reducer was used to reduce water usage by up to 40%, enhancing the workability as well as the compressive strength of the cement. Fine silica sand with an average diameter of 110 μm was used as fine aggregate, as recommended in [19] for better micro-mechanical properties of the ECC mix.

For the CB-ECC, CB particles Vulcan XC72R from Cabot Co. were used, which have a size of 30 nm and have a high bulk resistivity of around 10^{-1} Ω·cm. The content of CB was 1.0% by weight ratio to the total cementitious materials (cement and fly ash), which according to previous research could result in a balance in the mechanical and self-sensing performance of concrete [13, 14]. Details of the constituents of the ECC and their mass proportions are shown in Table 4.1.

Table 4.1 Composition of ECC mix

ECC mix	**Cement**	**Fly ash**	**Sand**	**Water**	**HRWR plasticizer**	**CB (%)**	**Fibre volume (%)**	
							PVA	**SF**
SF-ECC	1.0	1.2	0.8	0.56	0.012	-	1.75	0.58
CB-ECC	1.0	1.2	0.8	0.6	0.022	0.455	1.75	-

Note: HRWR = High-range water reducer

4.1.2 Specimen preparation

The mix procedure requires a high standard of even distribution of the fillers to achieve a relatively homogeneous cement matrix with the expected properties. In this study, the latter admixing method and synchronous admixing method were applied respectively for the SF-ECC and CB-ECC [6]. For the SF-ECC, the cementitious materials and silica sands were first dry mixed in a Hobart mixer for 2 min. Then one third of the water with super plasticiser was poured into the mixer to wet mix it for 1 min. When the mortar workability was judged adequate, the rest of the water was poured in with the steel fibres and PVA fibres were added gradually over 2 min. Finally, the mix was set in moulds and cured for 28 days, after which it was de-moulded. For the CB-ECC, the main difference was that the CB powders were blended with other dry materials initially before dry mixing. Since the CB particle size would decrease the workability of the mix, it required more time for moulding and vibration.

After curing of the SF-ECC and CB-ECC, the uniaxial compression test was conducted to assess the compressive strength of both types of ECC. Three cubic specimens with dimensions of 50 mm×50 mm×50 mm and three cylindrical specimens 100 mm in diameter and 200 mm in height were cast for each type of ECC. Testing was performed using a 500 kN Baldwin machine with the loading rates of 112.5 kN/min and 157.08 kN/min respectively for the cubic and cylindrical specimens, respectively in accordance with ASTM C39 standard [57]. The average compression strength was 45.02 MPa for SF-ECC and 40.98 MPa for CB-ECC. To test the flexural strength behaviour, beam specimens of both the SF-ECC and CB-ECC, each with the dimensions 350 mm ×100 mm ×100 mm,

were prepared for the four-point bending test. Additionally, thin plate-shaped specimens (300 mm×50 mm×12 mm) for SF-ECC and CB-ECC each were cast for tensile testing.

4.2 Resistance measurement

When the specimen was prepared, the specific electrical resistance measurement method needs to be determined as well. The simplest one is two-probe DC method where only one multimeter is sufficient for the circuit setup. A cubic specimen with dimensions of $50\ \text{mm} \times 50\ \text{mm} \times 50\ \text{mm}$ was used to check the feasibility of this approach by an Agilent 34461A multimeter. Two $5\ \text{mm} \times 5\ \text{mm}$ copper plates were attached in the middle of two opposite surfaces of the specimen as electrodes. The measurement for the resistance between these two points was conducted 3 times. Each time the measurement lasted for 1 min and the time interval between each measurement was 2 mins. The circuit setup and measurement results are shown in Figure 4.1. It is observed that, although the resistance for each time starts at a relative stable value, it increases rapidly at the start of measurement and keeps increasing until it reaches the 120 MΩ upper limit of the calibrate range of the multimeter. This is mainly because the polarisation effect. When the multimeter raises the measurement range and reaches a higher level of voltage, the resistance even jumped dramatically. In addition, two-minute recovery time is not enough for measurement for the same points. Therefore, the DC method is not suitable for a long-time continuous measurement, especially for some load tests which will last more than 10 mins.

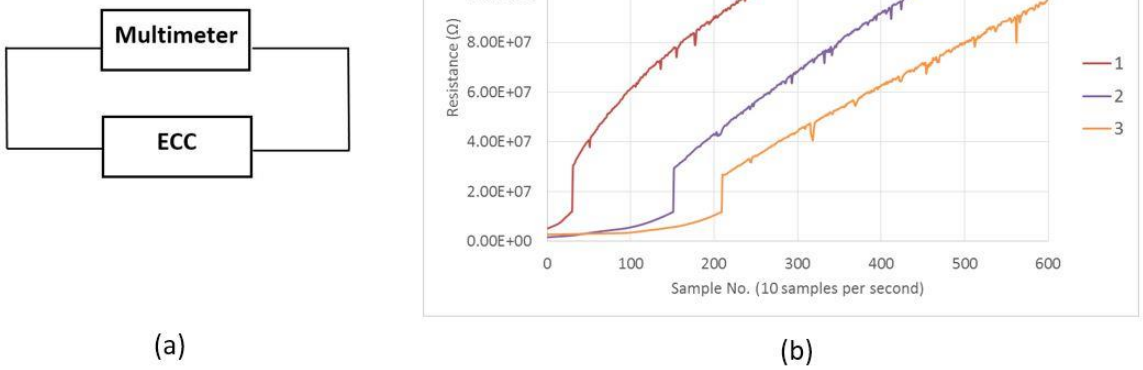

Figure 4.1 Two-point DC method: (a) instrument set up and (b) test measurement.

Two-probe AC method was then tested for the same specimen. A signal generator was added into the circuit in series to offer a constant frequency alternating electrical potential. The multimeter was set as an AC meter to calibrate the current trend. Since the frequency range of 1 Hz to 10 kHz can result in the least impact by the capacitance of ECC, the frequency of signal source was set as 5 kHz, and the amplitude was selected as ± 5 V. The instrument setup and the result for 1-min measurement is presented in Figure 4.2. The resistance fluctuates mildly within 0.1% and is much more stable than that of DC measurement, which demonstrated the feasibility of AC method for the following measurement. As for the probe layout, the contact impedance in two-probe layout is much lower than the quantity of resistance from ECC, which means that a four-probe method may be unnecessary for this study.

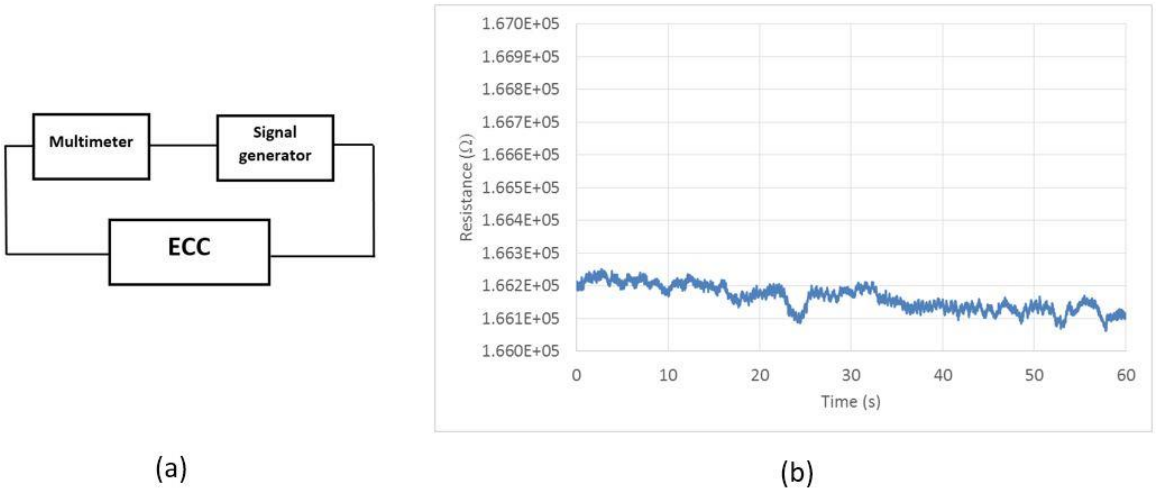

Figure 4.2 Two-point AC method: (a) instrument set up and (b) test measurement.

4.3 Discrete element method (DEM)

Simulation of the cracking behaviour of ECC requires a method that could track crack development and be suitable for anisotropic material. For this purpose, the DEM was adopted, which could simulate the motion and load effect of a large number of small particles. The DEM was first introduced by Cundall [58] for the analysis of rock-mechanics problems and developed to simulate granular and discontinuous material such as rock, soil and concrete [59-64]. In previous researches, the particle flow code (PFC) was commonly used for numerical simulation of DEM studies.

The model in DEM by PFC2D program is formed by a large number of particles and bonds, and the interaction between particles and bonds is treated as dynamic process with states of equilibrium developing whenever the internal forces balance. There are three types of contact stiffness models that can be selected: contact bond model, slip bond model and parallel bond model. The contact bond model uses a finite normal stiffness to measure the

stiffness between particles. The contact force and shear force are linearly relevant to the normal and shear stiffness. The slip bond model can be used to find the maximum shear force between particles with a friction coefficient. In the parallel bond model, the bond can transmit moment as well as force, and it cannot prevent slip of particles. It is more suitable to be applied for ECC simulations to realise the pull-out mechanism of fibres. The parallel bond model with two balls and one elastic beam is shown in Figure 4.3 [63].

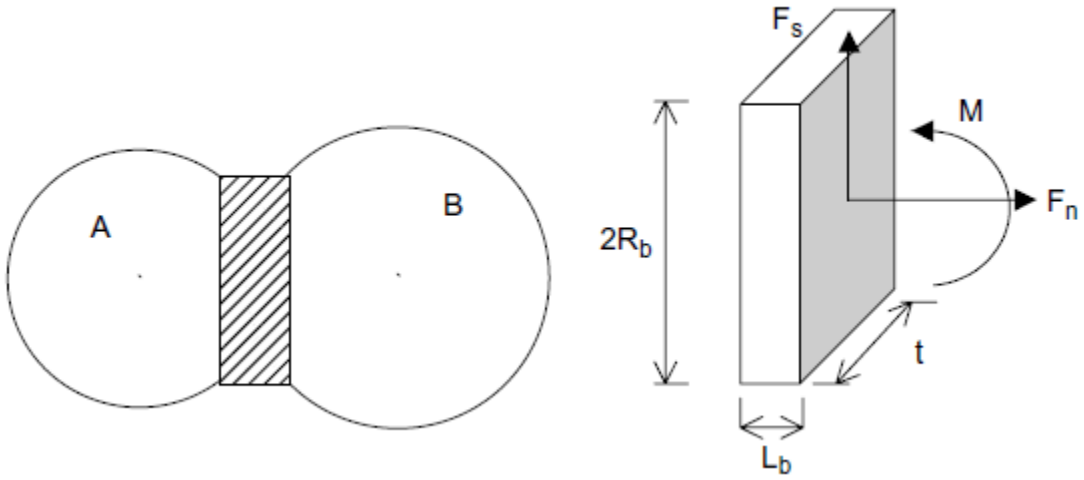

Figure 4.3 Parallel bond model and elastic beam.

Two basic laws are applied in the DEM for parallel bond model, i.e. Newton's second law for the contact motion between two particles, and the force-displacement law for updating the contact force generated by the relative motion of the particles. The contact force can be resolved into two directions, which are normal force F_n and shear force F_s

$$F = F_n + F_s \,, \tag{4.1}$$

$$F_n = k_n U_n \,, \tag{4.2}$$

where U_n is the normal displacement; k_n is the normal contact stiffness, which can be obtained as

$$k_n = \frac{k_n^1 k_n^2}{k_n^1 + k_n^2}, \tag{4.3}$$

where k_n^1 and k_n^2 are the contact normal stiffnesses of the two particles in the model, respectively.

The shear force is calculated in incremental fashion and is generated as zero when the bond was formed at the beginning. The incremental shear force is calculated as

$$\Delta F_s = -k_s \Delta U_s, \tag{4.4}$$

where ΔU_s is the shear displacement incremental; k_s is the contact shear stiffness given by

$$k_s = \frac{k_s^1 k_s^2}{k_s^1 + k_s^2}, \tag{4.5}$$

where k_s^1 and k_s^2 are the contact shear stiffnesses of the two particles in the model, respectively.

Then the normal force and shear force can be obtained by the accumulation of the increments for each time step from zero, such as

$$\Delta F_n = k_n A \Delta U_n, \tag{4.6}$$

$$\Delta F_s = -k_s A \Delta U_s, \tag{4.7}$$

where A is the area of the parallel bond cross-section, especially in PFC2D as

$$A = 2R_b t\,, \qquad t = 1\,, \tag{4.8}$$

$$R_b = \lambda \min(R^1, R^2), \tag{4.9}$$

where R_b is the parallel bond radius; R^1 and R^2 are the radii of the two particles respectively; λ is the bond-radius multiplier.

The twisting moment is treated as zero in the PFC2D model. For bending moment M_s calculation, the basic rules are similar as the calculation of force between balls in model, which can be given by

$$\Delta M_s = -k_n I \Delta\theta_s\,, \tag{4.10}$$

where I is the moment of inertia of parallel bond cross-section; $\Delta\theta_s$ is the rotation increment.

The maximum tensile and shear stresses resulted in the parallel bond can be calculated based on the beam theory as

$$\sigma_{max} = \frac{-F_n}{A} + \frac{|M_s| R_b}{I}\,, \tag{4.11}$$

$$\tau_{max} = \frac{|F_s|}{A}\,. \tag{4.12}$$

The parallel bond will break, if the maximum tensile stress exceeds the tensile strength or the maximum shear stress is larger than the shear strength. In that condition, the parallel bond can be removed from the model. With the use of a time-stepping algorithm in which the velocities and accelerations are assumed to be constant in each time step, the dynamic

behaviour of each particle can be traced, so that partial movement, deformation or fracture accumulates for the macro reaction of the whole object.

4.4 Artificial neural network (ANN)

ANN technique is a time saving, efficient and, more importantly, accurate computational method for solving complex nonlinear problems. ANNs are inspired by the sophisticated functionality of human brains, where many billions of interconnected neurons process data in parallel [65, 66]. This approach is an enthralling mathematical tool for solving complicated problems which are difficult to approach linearly. The neural network technique has been adopted and used to simulate a wide variety of complex problems in both science and engineering fields [67, 68]. In particular, the technique was successfully used to model the confined compressive strength and strain of concrete columns [69]. Some researchers modified the multi-layer ANN model to predict concrete strength and elastic modulus [70, 71]. The ANN technique was also applied to many other types of concrete, such as autoclaved aerated concrete [72], self-compacting concrete [73] and granulated blast furnace slag concrete [74].

Commonly, an ANN model consists of one input layer, two hidden layers (where the training occurs) and one output layer. Different numbers of neurons are required for the input and hidden layers for training and all layers are assigned to different transfer functions, e.g. tan-sigmoid, log-sigmoid and pure linear. The ANN model is then validated using an appropriate validation method such as k-fold validation or cross-validation.

An ANN model consisting of two hidden layers has been demonstrated to be adequate in most structural-related analysis [75]. The feedforward network consists of a series of layers

where each layer has a connection from the preceding one and the information passes through the network in the forward direction utilising the neuron connections within the layers [76]. In general, ANN models feature one input layer with a known value $i_p(p = 1,2,\dots m)$, two processing layers containing j and k neurons respectively, and one output layer with related parameters $o_s(s = 1,\dots\ ,n)$. The neurons are connected via the weight matrix and a set of biases. Mathematically, the s^{th} output variable, depicted in Figure 4.4, in the designed ANN model is calculated by [77]

$$\bar{o_s} = F_3\left(\left(\sum_{q=1}^{k} \bar{w}_{q-i}^{3} \cdot F_2\left(\left(\sum_{r=1}^{j} \bar{w}_{r-q}^{2} \cdot F_1\left(\left(\sum_{p=1}^{m} \bar{w}_{p-r}^{1} \cdot \bar{i}_p\right) + \bar{b}_r^1\right)\right) + \bar{b}_q^2\right)\right) + \bar{b}_i^3\right), \tag{4.13}$$

where $\bar{w}_{u-v}^{l}(l = 1,2,3)$ represents the weight connecting the u^{th} neuron in the l^{th} layer and the v^{th} neuron in the $(l+1)^{\text{th}}$ layer, while $\bar{b}_v^l$ and $n\bar{i}_v^l$ are the added bias and the net input in the l^{th} layer for the v^{th} neuron in the $(l+1)^{\text{th}}$ layer. $F_l(l = 1,2,3)$ is the transfer function for activating neurons in different layers [77].

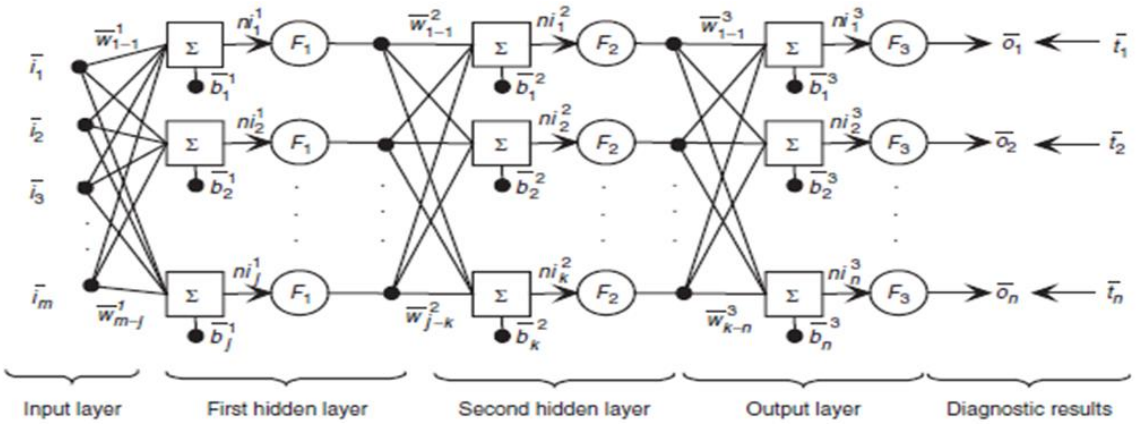

Figure 4.4 Feedforward ANN model with two processing layers [75].

The neural network can learn its weights and biases using the gradient descent algorithm, i.e. by repeatedly computing the gradient function ∇C, where C is a general function used in the neural network, and then moving in the opposite direction. The process is carried out until the descent algorithm reaches the desired value, e.g. a minimum. However, there is a gap where the gradient of the function can be difficult to obtain [78]. As a result, an algorithm known as backpropagation is used to provide a fast algorithm for computing such a gradient. Backpropagation is associated with a stochastic steepest descent algorithm for ANN training within a required error tolerance [75]. The mean square error function (MSE) E_r is defined as [77]

$$E_r = \frac{1}{n}\sum_{s=1}^{n}(\overline{t_s} - \overline{o_s})^2 \,, \tag{4.14}$$

where $\overline{t_s}$ is the s^{th} target vector and n is the total number of output vectors. In the training process, the weight and bias values are modified based on the steepest descent method in order to minimise the MSE, E_r [79]. Before the training proceeds, the selection of neuron numbers should be appropriately decided. The criterion for the numbers of neurons was suggested by Su and Ye [80] as

$$i = \sqrt{p + q} + B \,, \tag{4.15}$$

where i, p and q are the numbers of neurons, input components and output components for each processing layer, respectively. B is an empirical constant ranging from 4 to 8, depending on various applications of the model.

In the present study, the neural network training was accomplished by utilising the "Neural Network Toolbox – MATLAB" (R2016b). The transfer functions were selected to be Tan-

sigmoid and Log-sigmoid for the processing layers 1 and 2, respectively. The transfer function was set to be pure linear for the output layer so as to avoid limiting the output values to a small range.

The hyperbolic tangent sigmoid (Tan-sigmoid) transfer function, illustrated in Figure 4.5, has a mathematical expression of

$$f(x) = \frac{e^{x}-e^{-x}}{e^{x}+e^{-x}} , \tag{4.16}$$

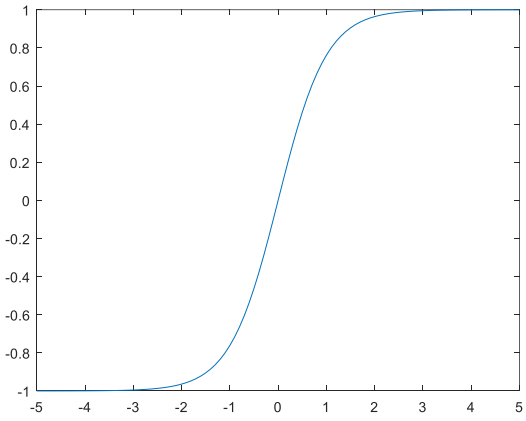

Figure 4.5 Tan-sigmoid transfer function.

while the log sigmoid transfer function, shown in Figure 4.6, can be expressed by

$$f(x) = \frac{1}{1+e^{-x}} . \tag{4.17}$$

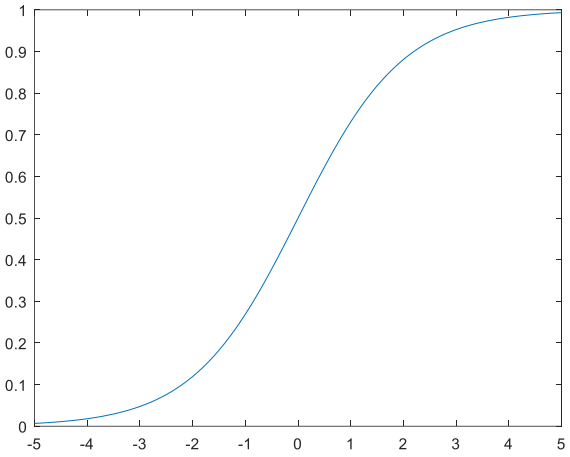

Figure 4.6 Log-sigmoid transfer function.

These two transfer functions acted as two separate step functions. The output will thus be 1 or 0 in the second hidden layer depending on the weight and bias in the neuron.

Finally, the pure linear function takes place after the hidden layer 2 in order to produce the final outputs. The pure linear function can be expressed by

$$f(x) = x\,. \tag{4.18}$$

4.5 ERT based on probabilistic diagnostic algorithm

4.5.1 ERT method

To construct ERT usually requires a proper electrode layout, whereby measurements can cover the proposed detection area. In the proposed method, each pair of electrodes can be treated as a single conductive pathway. With multiple sensing pathways and a damage index defined from the changes in electrical resistance, damage can be evaluated using a tomography approach with a 2-D algorithm. This approach is based on the following

assumptions: (1) damage (e.g. microcracking) can break down electrical conductivity in sensing pathways; (2) the growth of multiple microcracks increases electrical resistance; (3) for a specific conductive pathway, the greater the change in electrical resistance, the closer the pathway is to extensive microcracking or large defects [81]. Following these assumptions, a network of pathways can be set up to construct a 2-D image of damage areas (with extensive microcracking or large defects), indicating the possible location of severe damage such as cracks. The probability of the presence of crack presented as weighted change in electrical resistance at position (*x, y*) for each conductive pathway can be written as

$$p_k(x,y) = D_k \cdot W_k[r_k(x,y)]\,, \tag{4.19}$$

where D_k is the damage index ($=R_k/R_{k0}-1$, where R_{k0} and R_k are the electrical resistance before and after damage, respectively) of the *k-th* conductive pathway. $W_k[r_k(x,y)]$ is the weight given to the damage index of the *k-th* conductive pathway at *(x, y)*. $r_k(x,y)$ is the relative distance from point *(x, y)* to the *k-th* conductive pathway

$$r_k(x,y) = \frac{d_{s,k(x,y)} + d_{e,k(x,y)}}{d_k} - 1\,, \tag{4.20}$$

where d_k is the distance between the start point and end point of the *k-th* conductive pathway, $d_{s,k(x,y)}$ and $d_{e,k(x,y)}$ are the distances between point *(x, y)* to the start point and to the end point of the *k-th* conductive pathway, respectively. The weight increases when the relative distance decreases. It will peak at 1.0 once a point is located along the *k-th* conductive pathway. It is assumed that the weight follows a linear distribution function when the point is located on the affected zone which is specified by a scaling parameter β

(set as 0.05 in this study). Otherwise, the weight is set as zero. The weight function can therefore be established as

$$W_k[r_k(x,y)] = \begin{cases} 1 - {r_k(x,y)}/{\beta}, & r_k(x,y) < \beta \\ 0, & r_k(x,y) \geq \beta \end{cases}, \qquad (4.21)$$

Then, the probability of the existence of damage for each point in the monitoring area can be obtained by the accumulation of $p_k(x,y)$ for all the conductive pathways, as shown in Figure 4.7

$$P(x,y) = \sum_{i=1}^{k} p_i(x,y) \ . \qquad (4.22)$$

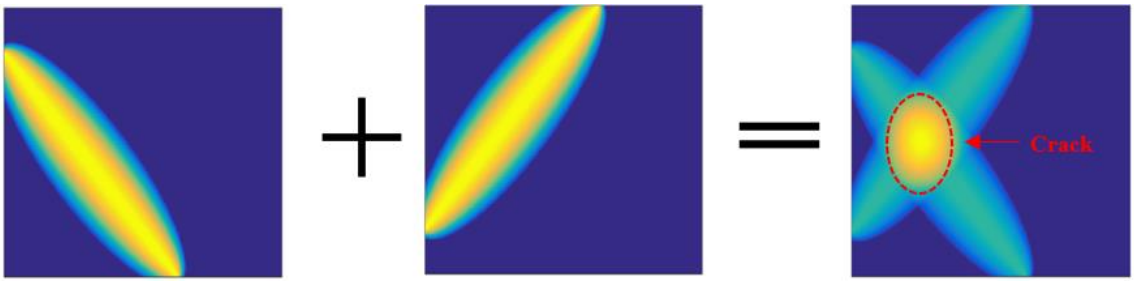

Figure 4.7 Potential damage area obtained by combination of individual ERTs of different conductive pathways.

Two schemes of data fusion were applied with the concept of conjunctive and compromised fusion in this study [82]. To be more precise, the intensity of the occurrence of damage for the point (x, y) for conjunctive data fusion can be obtained by the product of the weighted change in all conductive paths

$$P(x,y) = \prod_{i=1}^{k} p_k(x,y) \ , \qquad (4.23)$$

whereas the compromised data fusion can be expressed as

$$P(x,y) = \frac{1}{k}\sum_{i=1}^{k} p_k(x,y) \ , \tag{4.24}$$

By using these fusion methods, the effect of each conductive path will be balanced and will result in a more rigorous estimation for the damage pattern.

4.5.2 Preliminary test of ERT

In this study, some cubic specimens with dimension of $50\ \text{mm} \times 50\ \text{mm} \times 50\ \text{mm}$ have been tested to validate the accuracy of ERT by this method (Figure 4.8). The measurement was conducted by two-point DC method for process simplification and time saving. Since the polarisation effect of DC method will lead an increasing measured result for resistance, each conductive pathway was measured for 5 sec. And the value was taken as the average value during the measurement.

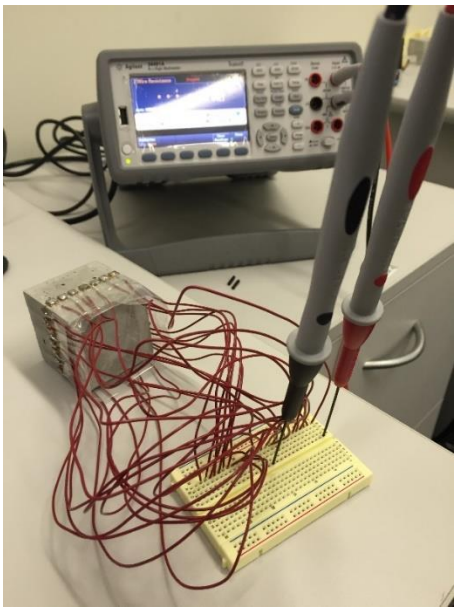

Figure 4.8 Measurement of ERT for cubic specimen.

The electrodes layout and conductive path way layout are shown in Figure 4.9, on which the red thick line is a cutting of 1mm thick and 5 mm depth. There are 8 conductive pathways in the oblique direction, 3 pathways in the vertical direction and 3 pathways in the horizontal direction, formed by selected pairs of electrodes. The ERT pattern for crack on the edge was analysed. In this way, the location with intensity values for the presence of damage above a specified threshold of probability can be defined as the damage area. The grid with the highest intensity value indicates the centre of the identified damage, as shown in Figure 4.10. The simple false-color filtering process were used to focus on compromised zones, which can help accurately determine the size of the crack area [83]. The critical region in the tomography shows a great consistency with the cutting point. However, the dimension of the crack cannot be well presented at the current stage. It is mainly due to the quantity of conductive path ways are not enough for much detailed representation.

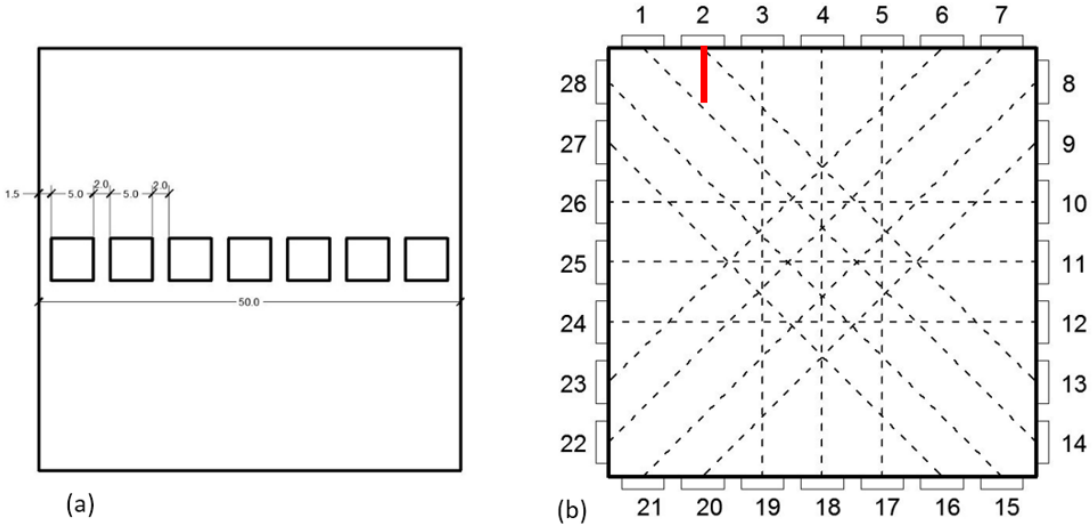

Figure 4.9 Test layout and setup: (a) Electrode position and (b) Conductive paths and cutting location.

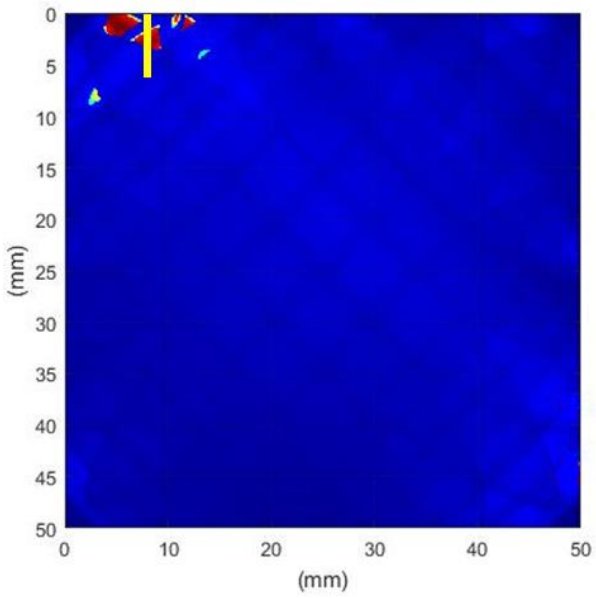

Figure 4.10 Crack localisation by ERT.

4.6 Summary

This chapter shows the ECC specimen preparation process and electrical resistance measurement method to be applied for the following studies. The principle of ANN was introduced to provide a gateway for ECC design and optimisation. DEM models and simulation process were reviewed for the further cracking study of ECC. And a proposed probabilistic algorithm for ERT was presented and proved feasible for ECC by some preliminary experiments.

Chapter 5 Property prediction of ECC by artificial neural network

In this chapter, several ANN models are developed correspondingly in order to predict the electrical and mechanical properties, such as resistivity, compressive strength, flexural strength and tensile strength, of some typical ECCs fabricated with PVA and SF. The datasets for ANN training are based on a comprehensive literature review of previous studies. A set of experiments including compression test, four-point bending test, tensile test and electrical resistance measurement for ECCs with various proportions of PVA and SF were conducted to demonstrate the capability of ANN models in predicting the mechanical and electrical properties of ECCs.

5.1 Artificial neural network

5.1.1 ANN set-up

In order to achieve property prediction, the neural network model needs to be trained first using the available datasets where different constituents of ECCs are considered as input and corresponding electrical and mechanical properties are considered as output. In this study, datasets for PVA-ECCs were based on a comprehensive literature review [8, 9, 19, 39, 66, 69, 84-87]. However, some of the data were blemished and thus were missing or zeroed. Therefore, after tailoring and regrouping the relevant data, 24, 44, 47 and 54 datasets were available, corresponding to different compressive strength, tensile strength, flexural strength and failure strain capacity, respectively, and were used as output for ANN training. Each dataset contained nine parameters that constituted PVA-ECC as input for

ANN training, i.e. weight of cement, class F and C fly ash, silica sand, coarse aggregates, crush sand, water, high-range water reducer, volume fraction of PVA. The input and target data were normalised with the maximum value into the range of [0, 1], while the weight and bias values were randomly initialised. An example of one set of input values for the model for compressive strength of PVA-ECC is shown in Table 5.1. Therefore, the total numbers of inputs were 216, 396, 423 and 486, respectively, and the total numbers of the target data (output) were 24, 44, 47 and 54, correponding to different mechanical properties to be predicted, respectively.

Table 5.1 Example of input data for ANN model training for PVA-ECC

Cement	**Class F fly ash**	**Class C fly ash**	**Silica sand**	**Crush sand**	**Coarse aggregate**	**Water**	**HRWR**	**PVA**
0.3	0.3	0.0	0.2	0.0	0.0	0.2	0.003	0.012

For the SF-ECC, the available datasets were also found in literature. In detail, there were 24 sets of constituent data corresponding to compressive strength [24]. The electromechanical behaviour of the SF-ECC had also been studied [26] and thus 12 sets of data were available with corresponding tensile strength, tensile strain and electrical resistivity values.

Correspondingly, the ANN models for predicting the mechanical properties featured one input layer with a proportion of the constituents of the composite, two processing layers containing *j* and *k* neurons respectively, and one output layer with related property values.

Determination of the number of neurons followed Equation (4.15). For the study of PVA-ECC, due to lack of sufficient data for a single training, four different ANN models were designated ANN_c, ANN_t, ANN_f and ANN_s, corresponding to compressive strength, tensile strength, flexural strength and failure strain capacity, respectively. These four ANN models were configured with the respective neuron numbers as shown in Table 5.2. In the case of SF-ECC there were two ANN models, ANN_{sfc} for compressive strength and ANN_{sfe} for resistivity, tensile strength and strain, with the corresponding numbers of datasets and neurons also given in Table 5.2.

Table 5.2 Number of neurons used in ANN model training for PVA-ECC and SF-ECC

	Available datasets for ANN training	**Number of neurons in the first layer**	**Number of neurons in the second layer**
ANN_c	24	23	6
ANN_t	44	34	9
ANN_f	47	34	9
ANN_s	54	35	10
ANN_{sfc}	24	25	12
ANN_{sfe}	12	15	8

The designated ANN models were set up for training, with the initialised weight and bias values assigned to neurons at different layers. The outcomes generated were then compared with the target values. After that, the backpropagation algorithm was applied to achieve an

accurate ANN model. Eventually, the ANN models were tested and validated with the Matlab built-in toolbox function to ensure their robustness.

5.1.2 ANN models and results

5.1.2.1 PVA-ECC

Each ANN model for PVA-ECC was trained with the total number of available datasets minus one to be used for validation. This process was carried out three times with new test data being replaced, and each process was performed six times and the averaged values were examined against the target value. The outcomes are shown in Tables 5.3-5.4, where it is evident that the differences between the actual and the predicted values are marginal for the PVA-ECC ANN models.

Table 5.3 ANN model training for compressive strength and flexural strength of PVA-ECC

	Compressive strength (MPa)	**Compressive strength (MPa)**	**Compressive strength (MPa)**	**Flexural strength (MPa)**	**Flexural strength (MPa)**	**Flexural strength (MPa)**
Prediction	**ANN_{c1}**	**ANN_{c2}**	**ANN_{c3}**	**ANN_{f1}**	**ANN_{f2}**	**ANN_{f3}**
Average	67.71	67.10	69.59	11.97	12.98	12.46
Target	67.7	69	67	11	12	12.68
Difference (%)	0%	3%	4%	9%	8%	2%

Table 5.4 ANN model training for tensile strength and failure strain capacity of PVA-ECC

	Tensile strength (MPa)	**Tensile strength (MPa)**	**Tensile strength (MPa)**	**Strain capacity**	**Strain capacity**	**Strain capacity**
Prediction	**ANN_{t1}**	**ANN_{t2}**	**ANN_{t3}**	**ANN_{s1}**	**ANN_{s2}**	**ANN_{s3}**
Average	5.40	4.24	4.05	3.48	3.24	3.64
Target	5.93	4.25	3.73	3	3	4
Difference (%)	9%	0%	9%	16%	8%	9%

In the model training, for instance for ANN_c, 70% (i.e. 16) of the samples were used for training, 15% (i.e. 4) for validation and 15% (i.e. 4) for testing. The error histogram illustrated in Figure 5.1 demonstrates the network performance, where the blue bars represent training data, the green bars represent validation data, and the red bars represent testing data. The error histogram gives an indication of outliers, which are data points where the fit is significantly worse than the majority of the data [77]. As shown in Figure 5.1 for ANN_c, all errors fall between -0.06415 (-6.4%) and 0.1102 (11%), indicating a quite trivial error. The other three networks also showed marginal errors, which are not shown here. Another index demonstrating the performance of the ANN model was MSE, as shown in Figure 5.2 for the case of failure strain capacity prediction, where the MSE converges to a constant level, indicating that the errors were minimised. Therefore, it was concluded that

the proposed ANN models were well trained and accurate enough to predict the mechanical properties of PVA-ECC.

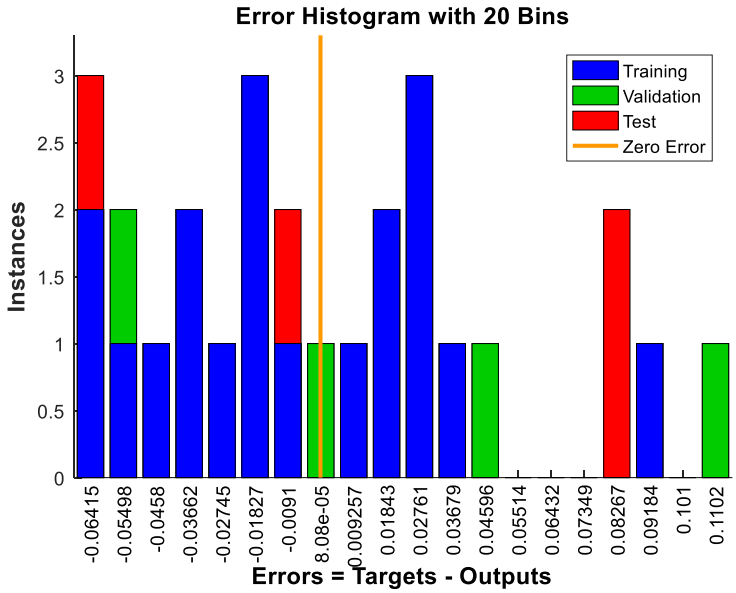

Figure 5.1 Error histogram with 20 Bins - ANNc as an example.

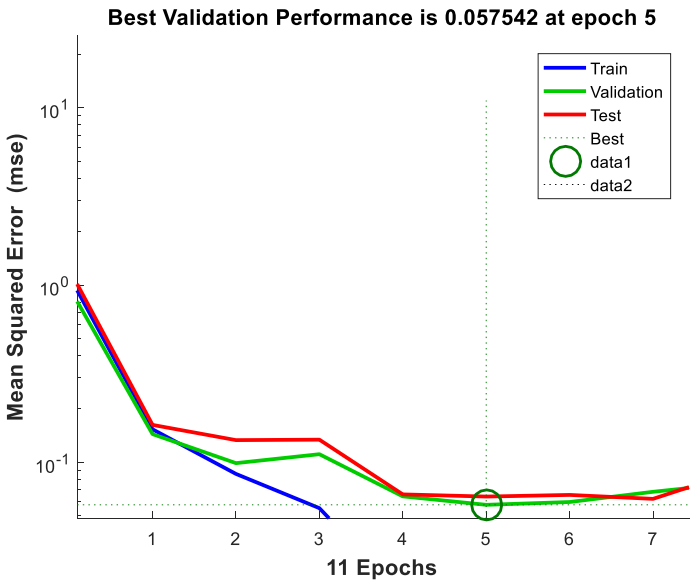

Figure 5.2 Convergence history of ANN training.

5.1.2.2 SF-ECC

Similar training of ANN models for SF-ECC was carried out, where the process was performed six times and the averaged values were compared with the target value. However, due to the lower amount of available data, only one dataset was extracted for validation against the target value. The outcomes for ANN_{sfc} and ANN_{sfe} are tabulated in Table 5.5. It is evident that the differences are also insignificant for the SF-ECC ANN models, indicating that quantitative prediction of the mechanical and electrical properties of SF-ECC could be satisfactorily achieved by these well-trained ANN models. It is also worth noting that, unlike other neural network models, the model ANN_{sfe} used to predict the electromechanical behaviour of SF-ECC, as shown in Table 5.5, could generate three outputs simultaneously for prediction, namely tensile strength, tensile strain and electrical resistivity.

Table 5.5 ANN model training for SF-ECC

	Compressive strength (MPa)	**Tensile strength (MPa)**	**Tensile strain**	**Electrical resistivity (kΩ）**
Prediction	**ANN_{sfc}**	**ANN_{sfe}**	**ANN_{sfe}**	**ANN_{sfe}**
Average	44.31	12.37	0.531	80.71
Target	42.40	12.14	0.540	80.08
Difference (%)	4.5	1.87	1.62	0.79

5.2 Experimental verification

5.2.1 Material selection

In order to verify the feasibility of the ANN models developed in Section 5.1 for property prediction, PVA-ECC and SF-ECC specimens with different compositions of PVA and SF which are not included for ANN training were prepared and tested, so as to compare with the predicted results from corresponding ANN models. The volume fractions of PVA for PVA-ECC were selected as 1%, 1.5% and 2%. The SF-ECC was fabricated with 1.75% volume fraction of PVA and 0.58% volume fraction of SF which was coppered micro steel fibres WSF0213. The material selection and properties were the same as those introduced in Chapter 4.1. The detailed constituents and their mass proportions are listed in Table 5.6.

Table 5.6 Composition of ECC mix

ECC mix	Cement	Fly ash	Sand	Water	HRWR	Fibre volume (%)	
						PVA	SF
SF-ECC	1.0	1.2	0.8	0.56	0.012	1.75	0.58
PVA-ECC-1	1.0	1.2	0.8	0.6	0.022	1	-
PVA-ECC-1.5	1.0	1.2	0.8	0.6	0.022	1.5	-
PVA-ECC-2.0	1.0	1.2	0.8	0.6	0.022	2	-

5.2.2 Specimen preparation and test set-up

The quantities of the specimens are listed in Table 5.7 according to different mechanical tests. Three cylindrical specimens of 100 mm in diameter and 200 mm in height were cast for each type of ECC for the compressive test. The test was performed by a 500 kN Baldwin machine (Figure 5.3(a)) with a loading rate of 157.08 kN/min, in accordance with ASTM C39 standard [57]. To test the flexural strength behaviour, three beam specimens of the PVA-ECC with the dimensions 4000 mm×100 mm ×100 mm were prepared for the four-point bending test. The test procedure followed the instructions in ASTM C78 standard [88] and the Baldwin 500 kN testing machine with displacement control was used with the loading rate set at 0.5 mm/min as recommended by the standard as shown in Figure 5.3(b). The failure strain capacity was obtained by the calculation based on the mid-point vertical deflection [89]. Additional eight thin plate-shaped specimens (300 mm×50 mm×12 mm) for PVA-ECC and SF-ECC each were cast for tensile testing, which was conducted on the Baldwin 500 kN testing machine (Figure 5.3(c)).

Table 5.7 Specimens for experiments

ECC mix	Cylinder	Beam	Plate
SF-ECC	3	-	8
PVA-ECC-1	3	3	8
PVA-ECC-1.5	3	3	8
PVA-ECC-2.0	3	3	8

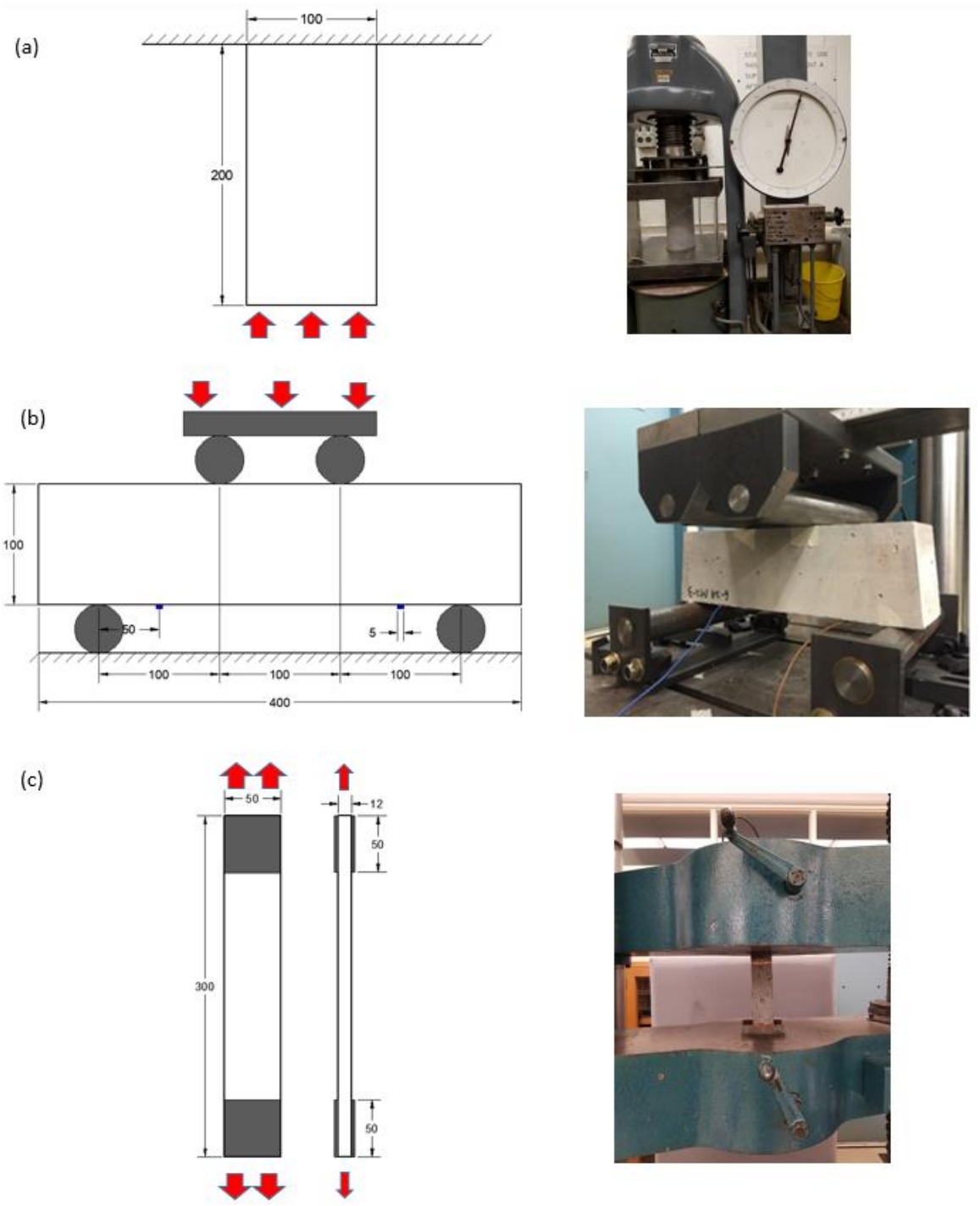

Figure 5.3 (a) Compressive test set-up; (b) Four-point bending test set-up and (c) Tensile test set-up.

During the flexural test, the two-probe AC method was adopted for electrical resistivity measurement, which could minimise the polarisation effect of resistivity by change in the electrical potential [46, 47, 90]. Two copper tapes (from 3M) of 0.5 cm in width were attached as electrodes. Silver conductive paste from RS was added between the tape and beam to improve the contact surface. A signal generator Tektronix AFG3102 was added into the circuit in series to provide a constant frequency alternating electrical potential. The Agilent 34461A multimeter was set as an AC meter to calibrate the current trend. The frequency of the signal source was set at 5 kHz and the amplitude was selected as ±5 V as justified in Chapter 4. As the environmental temperature has an approximately 3%/°C influence on resistance measurement, all the tests were conducted at the room temperature of 22 °C.

5.2.3 Experimental results

Three cylinders for each volume fraction (1%, 1.5% and 2%) of PVA-ECC (nine cylinders in total) were tested to obtain the respective compressive strength, with the averaged values at 58.94 MPa, 62.83 MPa and 57.4 MPa, respectively. The averaged experimental compressive strengths of the PVA-ECC are compared with the ANN predictions in Table 5.8. It is obvious that the results are quite close to those predicted from the ANN, in the range between 0.84% and 2.15%, and this demonstrates the feasibility and capability of the well-trained ANN model to predict the mechanical properties of ECCs.

Table 5.8 Experimental verification for ECC specimens

		ANN model	Prediction average	Experiment average	Difference (%)
PVA-ECC	Compressive strength (MPa)	ANNc-1	58.94	60.23	2.15
		ANNc-1.5	62.83	63.74	1.43
		ANNc-2	57.40	57.89	0.84
	Tensile strength (MPa)	ANNt-1	3.86	3.98	3.02
		ANNt-1.5	4.47	4.524	1.19
		ANNt-2	3.97	4.076	2.60
	Flexural strength (MPa)	ANNf-1	9.41	9.95	5.46
		ANNf-1.5	11.01	11.31	2.62
		ANNf-2	9.85	10.19	3.30
	Strain capacity (%)	ANNf-1	2.86	2.58	10.85
		ANNf-1.5	3.67	4.07	9.83
		ANNf-2	3.31	3.57	7.28
SF-ECC	Compressive strength (MPa)	ANN_{sfc}	42.4	43.57	2.69
	Tensile strength (MPa)	ANN_{sfe}	4.68	4.57	2.41
	Electrical resistivity （kΩ）	ANN_{sfe}	149	149.91	0.61

In parallel, beam and plate-shaped specimens were tested to verify the flexural and tensile strengths. The averaged flexural strengths of PVA-ECC obtained in experiments were 9.95 MPa, 11.31 MPa and 10.19 MPa for 1%, 1.5% and 2% volume fraction respectively. The flexural strengths of the PVA-ECC predicted by the ANN_f models are also compared with the experimental results in Table 5.8, showing high consistency. Table 5.8 also compares the predictions and experimental results of tensile strength of the PVA-ECC, where the difference is even smaller, showing reliable prediction. As well, failure strain capacity is compared in Table 5.8, where the averaged difference is 9.32%, greater than the other models but still acceptable.

As with PVA-ECC, experimental results are compared with the predictions by ANN for SF-ECC in Table 5.8, where three cylinders and eight plate-shape specimens were tested. The difference between measurement and prediction was around 2.5% for both compressive and tensile strengths. The results for electrical resistivity showed better prediction as well, with a difference of 0.61% between experimental measurement and ANN prediction, implying a high potential of ANN for electrical design optimisation.

5.3 Discussion

It is understood that the ANN model may overfit when the number of neurons is above a certain threshold, whereas the presence of too few neurons in each layer can result in a poor training performance. Determination of the number of neurons in each processing layer in this study was based on Equation (4.15) for the ANN training which provides a reasonable range for the selection of neuron numbers to prevent the occurrence of abovementioned issues [75, 80]. Consistent results in terms of prediction accuracy have

been found by changing the number of neurons in each layer based on Equation (4.15), which verified its robustness.

Another factor influencing the precision of the prediction of mechanical properties in ECCs is the size of the database. The smaller the database, the less accurate the neural network can be and thus the less likely that the neural network can be used for the prediction of all properties. However, it is difficult to obtain complete and sufficient datasets from the literature. Therefore, it is strongly recommended that researchers conduct supplementary experiments for data collection, so that the ANN model can be used for the prediction of multiple properties.

It is also highly recommended to control the range of types of material that are adopted for training ANN models. A variety of commonly used constituents as different inputs should be employed into the ANN model. For instance, different types of superplasticizer and different batches of class F fly ash that may result in different mechanical properties of ECCs can also be included for training. Nevertheless, a comprehensive ANN model with sufficient datasets should be able to predict mechanical and electrical properties given that it is well trained and validated.

In this study, ANN models were developed to provide a convenient and transparent tool which enables engineers to predict and obtain the proposed design properties of ECCs by simply adjusting the input data in the model, i.e. material constituents. However, it is noteworthy that a detailed design based on micro-mechanic and fracture mechanic theories is still necessary to fully understand the mechanism behind the mechanical and electrical properties that ECCs demonstrate.

5.4 Summary

Prediction of mechanical and electrical properties of ECCs was developed by the ANN technique in this study. ANN models for PVA-ECC and SF-ECC were trained and validated based on collected data from existing researches. Series of experimental tests were conducted to assess the capability of the well-trained ANN models. The small differences between the predictions and tested values indicated that estimation of the mechanical and electrical properties of ECCs using ANNs could be achieved with good accuracy, benefiting the ECC design with desirable properties.

It was noted that the diagnostic performance and precision of the ANN models were highly dependent on the network configurations and structure. In summary, feedforward neural networks equipped with two processing layers and appropriate numbers of neurons using a backpropagation algorithm exhibited adequate capability of predicting the properties of ECCs given the proportion of its constituents.

Due to the lack of sufficient datasets, several different ANN models were developed in this study. There is still room to improve overall performance of the models with the addition of new datasets. One of the suggestions for future work is to carry out a number of experimental investigations to collect reliable data so that the ANN model to be developed is capable of predicting all the required mechanical and electrical properties in a single model.

Chapter 6 Self-sensing properties of engineered cementitious composites

In this chapter, mechanical and electrical properties of steel SF-ECC and CB-ECC are investigated. Four-point bending and uniaxial tensile tests synchronising AC resistance measurement were implemented to obtain stress-strain relationships and electrical resistance, which were correlated with cracking development. In parallel, DEM was applied to simulate the development of crack density during flexural and tensile testing.

6.1 Experimental study

6.1.1 Experimental setup

SF-ECC and CB-ECC specimens were prepared following the steps introduced in Chapter 4. The constituent and composition of materials were shown in Table 4.1. Three beam specimens of both the SF-ECC and CB-ECC, each with the dimensions 350 mm ×100 mm ×100 mm, were prepared for the four-point bending test. Additionally, three thin plate-shaped specimens (300 mm×50 mm×12 mm) for SF-ECC and CB-ECC each were cast for tensile testing. The four-point bending test was implemented with synchronisation of the electrical measurement, as shown in Figure 6.1. The test procedure followed the instructions in ASTM C78 standard [88] and the Baldwin 500 kN testing machine with displacement control was used with the loading rate setting of 0.5 mm/min as recommended by the standard. During the four-point bending test, the two-probe AC

method was adopted for electrical resistivity measurement, which could minimise the polarisation effect of resistivity by the change of the electrical potential [46, 47]. Two copper tape electrodes (from 3M) of 5 mm width were attached to the bottom surface. Silver conductive paste was added between tape and beam to improve the contact surface. A signal generator was added into the circuit in series to provide a constant frequency alternating electrical potential. An Agilent 34461A multimeter was set as an AC meter to calibrate the current trend. Following the same principle, the frequency of the signal source was set at 5 kHz, and the amplitude of ±5 V was selected. As the environmental temperature has approximately 3%/°C influence on the resistance measurement [91], the tests were conducted at the room temperature of 22 °C.

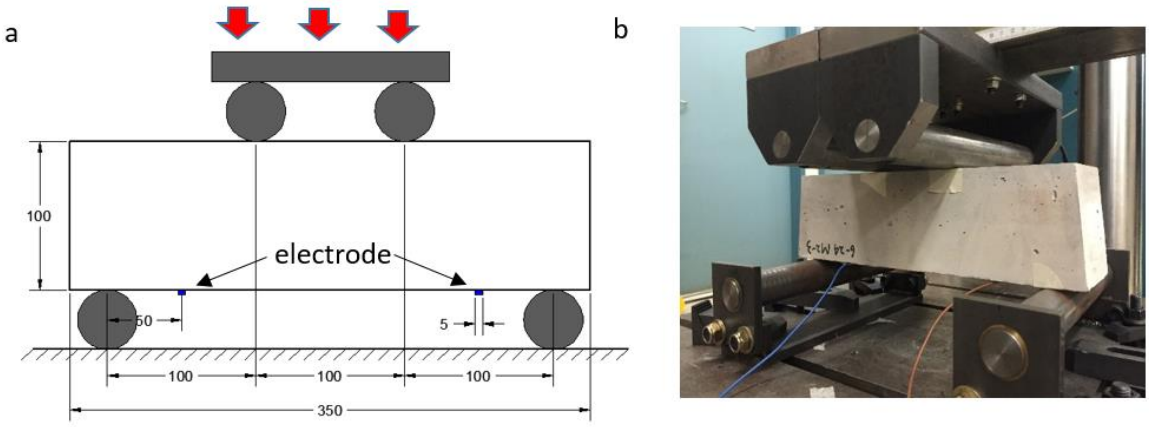

Figure 6.1 Four-point bending test with electrical measurement (a) geometry and (b) setup.

The experimental setup for the uniaxial tensile test is shown in Figure 6.2. To prevent stress concentration at the grip surface, thin aluminium plates (50 mm×50 mm) were stuck to the ends of the specimens by epoxy (ARALDITE® 420 A/B). The tests were conducted on the Baldwin 500 kN testing machine with displacement control. Since there is no specific standard for uniaxial tensile testing of cementitious materials, the displacement rate of 0.5

mm/min was used based on literature [15]. To acquire a more accurate measurement of elongation, a laser extensometer was used with the gauge length of 100 mm. For electrical resistance measurement, the same method and procedure were applied as in the four-point bending test. The measurement range of resistance was 150 mm at the middle of the specimen.

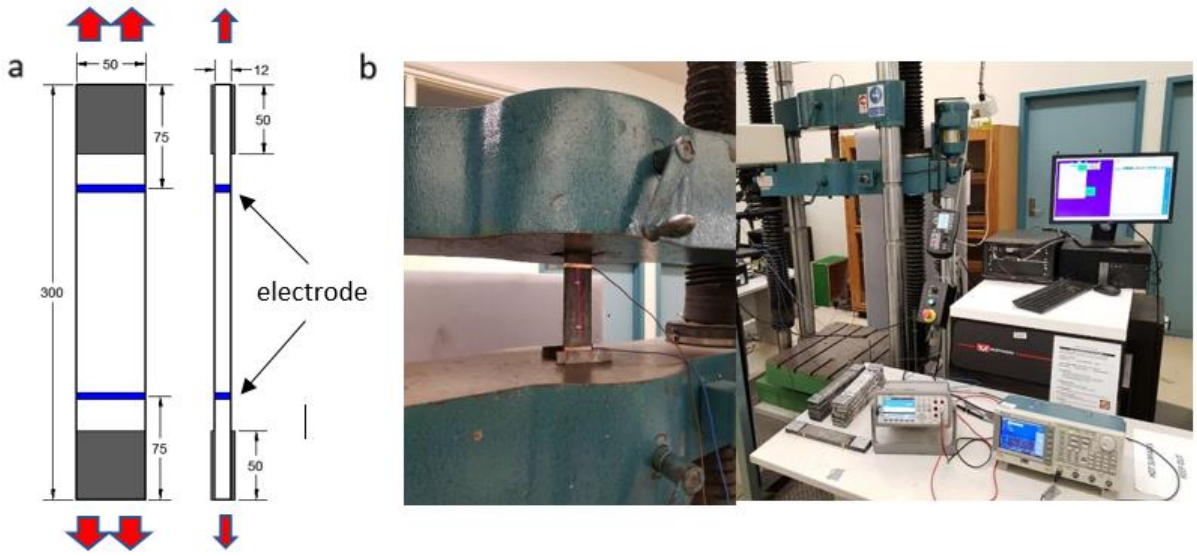

Figure 6.2 Uniaxial tensile test with electrical measurement (a) geometry and (b) setup.

6.1.2 Test results

6.1.2.1 Flexural test

Three beams each for SF-ECC and CB-ECC were tested. The flexural stress-strain curves at mid-span for the beams are shown in Figure 6.3(a). The dashed lines represent the stress-strain relationship for SF-ECC, which shows higher stiffness but lower failure strain than CB-ECC, denoted by solid lines. The modulus of rupture of SF-ECC is in the range between 9.93 MPa and 11.46 MPa, with the strain capacity varying from 2.00% to 2.23%.

For CB-ECC, the modulus of rupture is approximately half that of SF-ECC, between 5.48 MPa and 6.15 MPa, and the strain capacity is slightly higher, from 2.13% to 2.46%.

Since the PVA fibre content was the same for these two ECC types, the difference in flexural behaviour should be mainly caused by the different mechanical properties of SF and CB powders. The SF had high tensile strength of about 2600 MPa and could serve as reinforced tensile fibres with the aid of PVA fibres. The long fibre shape would also result in a pull-out mechanism. Even if micro-cracks occurred initially, the steel fibres would still resist tensile stress between the failure surfaces unless they were fully pulled out from the cement matrix. In contrast, the CB particles could only enhance the cement paste, producing limited improvement in flexural performance.

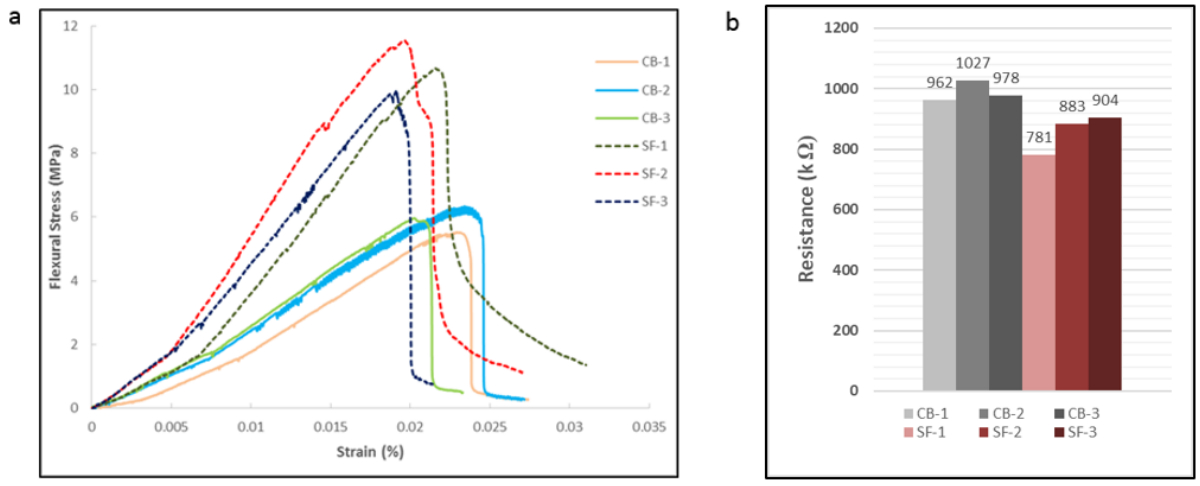

Figure 6.3 (a) Flexural stress-strain curves for SF-ECC and CB-ECC beams; (b) Resistance at bottom surface before major crack.

Figure 6.3(b) shows the resistance at the bottom surface for both ECC types before major cracks occurred. The resistance for SF-ECC ranges from 781 kΩ to 904 kΩ, whereas the

resistance for CB-ECC is about 962 kΩ to 1027 kΩ. The average resistive performance of the CB-ECC is nearly 15.54% higher than that of SF-ECC, indicating better conductivity enhancement by the SF than by the CB. There are two reasons for this difference. First, the conductivity of steel is relatively higher than that of CB. More importantly, the SF occupied a longer distance in the effective conductive paths. If the cement matrix and functional fillers are treated as a circuit in series for one conductive path, the charges would transport more areas in the cement matrix in the CB-ECC than in the SF-ECC given the same distance. As an accumulated effect of all the conductive paths, the overall conductive capacity of CB-ECC was lower than that of SF-ECC.

Figures 6.4(a) and 6.4(b) are the stress-strain curves and resistance-strain curves of one SF-ECC beam and one CB-ECC beam as examples in respective experiments. As the beam reaches failure, the resistance shows a rapid increase for each type of ECC beam. The major difference is that the resistance change in the CB-ECC is sharper than that in the SF-ECC before failure. Moreover, the resistance change at failure of the CB-ECC (124%) is greater than that of the SF-ECC (56%). This is mainly due to the different shapes of the materials. Once the beam approaches failure, the fibre shapes of SFs are more easily pulled out from the fracture surfaces rather than broken in the middle. Therefore, the SFs can still form conductive pathways until they are fully dragged out, and that can lead to a lower increase in resistance of the SF-ECC beam before failure.

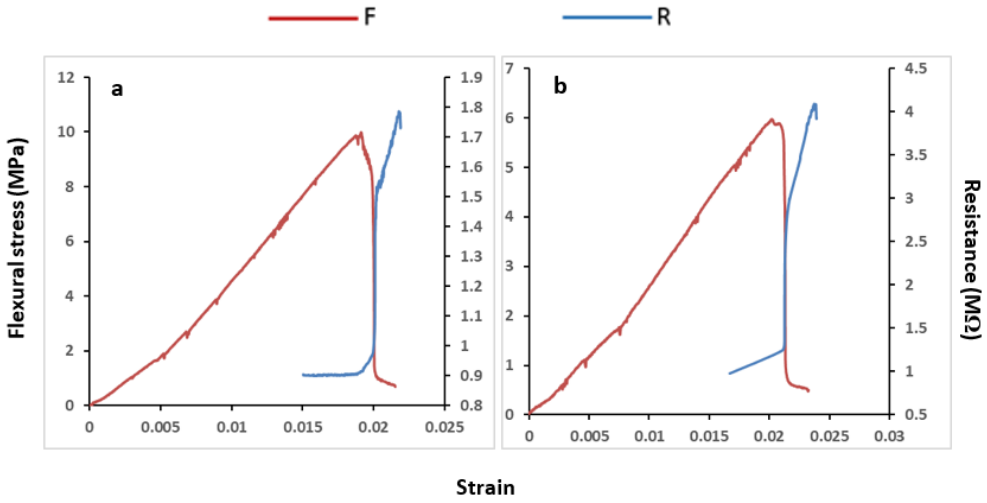

Figure 6.4 Stress-strain curve and bottom surface resistance-strain curve for four-point bending test of (a) SF-ECC; (b) CB-ECC.

6.1.2.2 Uniaxial tensile test

Tensile tests were conducted on three plate-shaped specimens of both SF-ECC and CB-ECC. The tensile stress-strain curves are shown in Figure 6.5(a). The tensile strength of the SF-ECC ranges between 5.10 MPa and 5.82 MPa, with the strain capacity varying from 1.78% to 2.18%. The tensile strength of the CB-ECC, which is between 2.64 MPa and 4.64 MPa, is lower than that of SF-ECC, and the strain capacity ranges from 1.65% to 2.37%.

The resistance for both types of ECC before major cracks occur is shown in Figure 6.5(b). The resistance for the SF-ECC ranges from 896 kΩ to 924 kΩ, whereas the resistance for the CB-ECC ranges from 987 kΩ to 1121 kΩ. As in the bottom surface resistance measured during the flexural test, the average resistance of the CB-ECC is 15.27% higher than that of the SF-ECC.

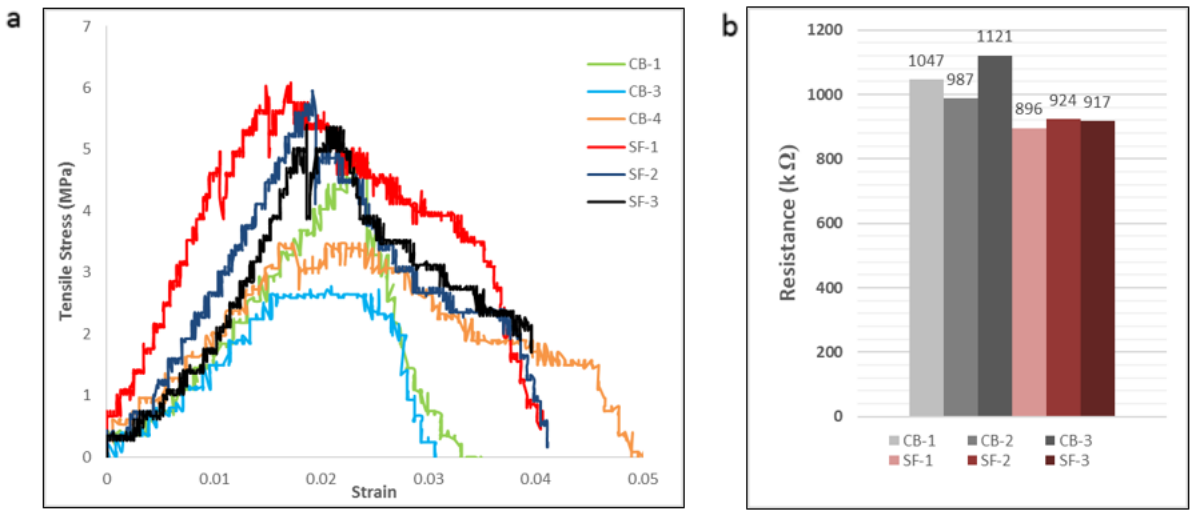

Figure 6.5 (a) Tensile stress-strain curve for SF-ECC and CB-ECC plates; (b) Resistance before major crack.

The stress-strain curves and resistance-strain curves of one SF-ECC plate and one CB-ECC plate as examples in experiments are presented in Figure 6.6. In the elastic range, the resistance of SF-ECC remains quite stable, whereas the resistance of CB-ECC begins to increase slightly with an increasing gradient. As the plate approaches failure, the resistance of SF-ECC begins to increase rapidly while the gradient decreases, until the resistance again dramatically increases when the specimen reaches the end of the strain-hardening state. In the CB-ECC, as the specimen approaches failure, the resistance continues to increase significantly until the final stage, a finding which indicates higher sensitivity to mechanical failure although the gradient decreases, as in the SF-ECC.

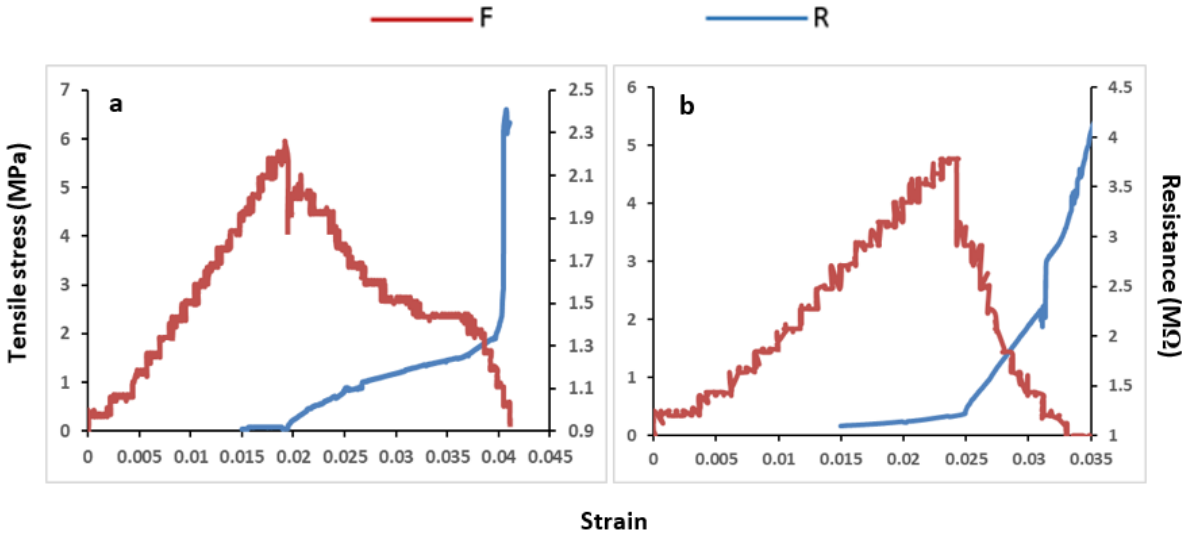

Figure 6.6 Stress-strain curve and resistance-strain curve for uniaxial tensile test of (a) SF-ECC; (b) CB-ECC.

6.2 Numerical simulation

6.2.1 DEM models

PFC in two dimensions (PFC 2D) was applied in this study. The model formed in PFC 2D is composed of circular particles with finite mass. These particles can move independently and only interact with each other at contacts. In the initial stage, the particles are connected by bonds of finite stiffness and strength at contacts. The strength of the bonds dominates the strength of the whole model, while cracking development can be reflected by the accumulation of bond failure.

For the four-point bending test, a rectangular model with length 350 mm and height 100 mm was built, consisting of 18481 particles and 0.58% clumps to simulate steel fibres for the SF-ECC. The PVA fibres and CB particles were not modelled, because their

dimensions compared with the particle size for the initial model were much smaller. The enhancement by PVA and CB would be reflected by the improved bond strength. Four circular particles of 30 mm radius were placed at the top and bottom to present roller footing and loading points. A wall with downward velocity of 0.5 mm/min was set as the loading platen to conduct the displacement-controlled four-point bending test. For the uniaxial tensile test, rectangular models 200 mm in length and 50 mm in width were set up to simulate the parts of specimens in tension. All the properties of particles and bonds (Table 6.1) were set according to data from a previous study by other researchers [92] which showed high consistency with the experimental results.

Table 6.1 Micro parameters for PFC 2D Models

Micro parameters	Values
Density	2036 kg/m3
Ball-ball contact modulus	23.1 GPa
Ball stiffness ratio (kn/ks)	2.5
Parallel-bond radius multiplier	2
Parallel-bond modulus	1 GPa
Parallel-bond stiffness ratio	1
Ball friction coefficient	0.5
Parallel-bond normal strength, mean	24 MPa
Parallel-bond normal strength, s.d.	±4.8 MPa
Parallel-bond shear strength, mean	24 MPa
Parallel-bond shear strength, s.d.	±4.8 MPa

6.2.2 Results and discussion

6.2.2.1 Flexural test

The sensitivity of self-sensing capacity in this study focused mainly on crack detection. The resistance at bottom surface of each beam specimen was measured during the four-point bending test with an increase in load. The curve for resistance development was correlated with the stress-strain curve so as to observe cracking state, together with comparison with the simulated cracking development in DEM.

For the SF-ECC beam, the post-cracking crack patterns with load, number of cracks, and flexural stress in terms of strain from numerical simulation are shown in Figures 6.7(a) and (b). It can be seen that the first micro-crack appears before the model reaches its flexural strength, and the number of cracks increases gradually with the increase in load. When the beam reaches failure point, the crack density jumps dramatically, at which time a visible major crack in the middle of the beam is generated. Since the test is under displacement control, the time-dependent stress change is almost the same as strain-dependent stress change. Compared with the experimental result, the moduli of rupture are both near to 11 MPa, and the trends of the stress curves are similar, which verified the numerical model. Therefore, the electrical measurement result was combined with crack number simulation domain by strain (Figure 6.9(a)). The simulated crack density development and the change in resistance during the test also show similar variation trends. Before the sharp increase in crack numbers which corresponds to the failure point of the beam, there is no apparent increase in the resistance. After that, the resistance grows dramatically with the increase in crack density. Finally, the rate of increase becomes mild in the post-cracking state. For the

CB-ECC beam, the simulation results shown in Figures 6.7(c) and (d) also demonstrate a lower failure strength than the SF-ECC beam, as in the experiments. As in the SF-ECC beam, the resistance change also demonstrates high sensitivity to crack development as shown in Figure 6.9(b).

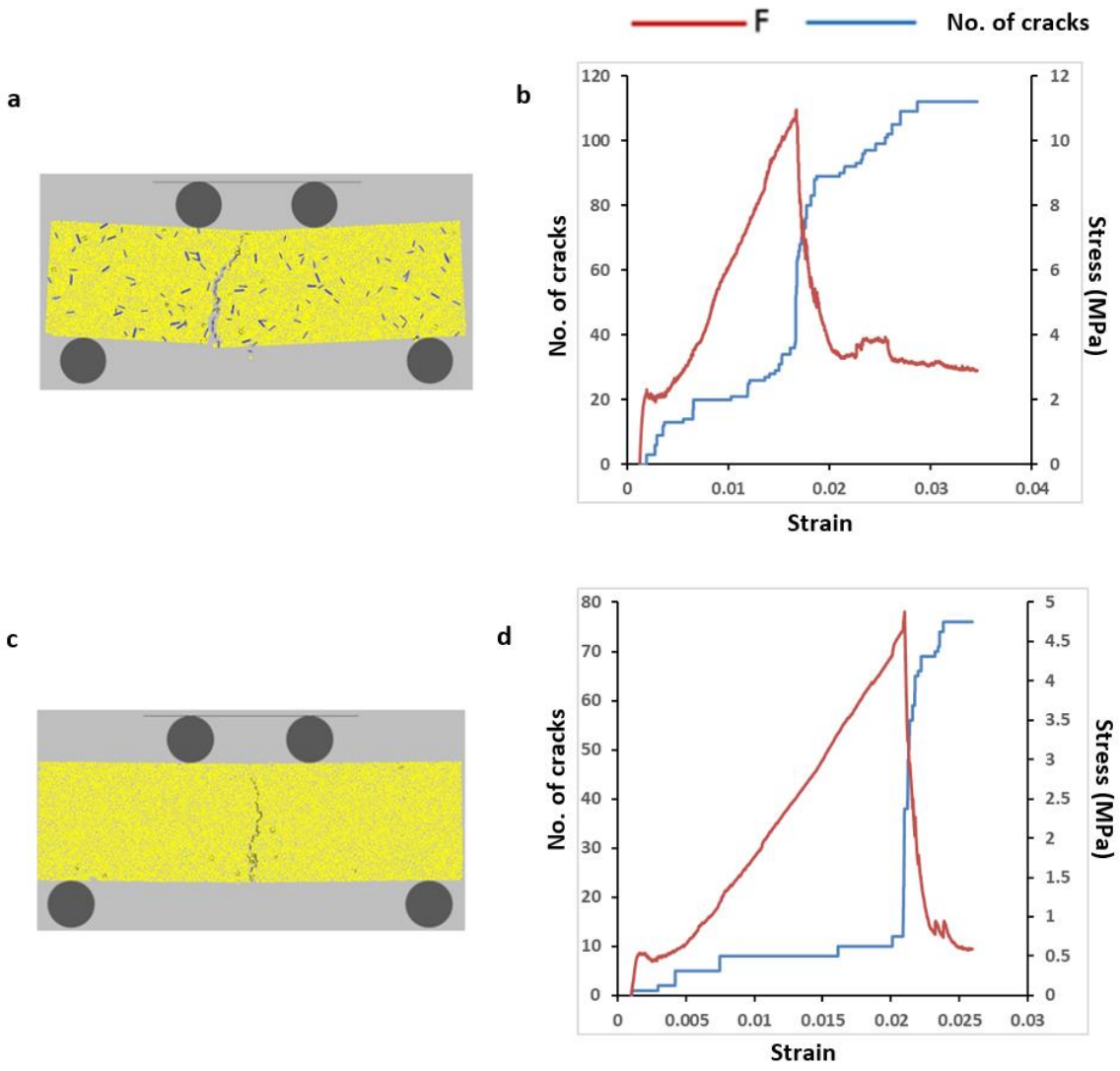

Figure 6.7 a) Post-cracking crack pattern of SF-ECC; (b) Flexural stress/micro-crack number vs strain for SF-ECC; (c) Post-cracking crack pattern of CB-ECC and (d) Flexural stress/micro-crack number vs strain for CB-ECC.

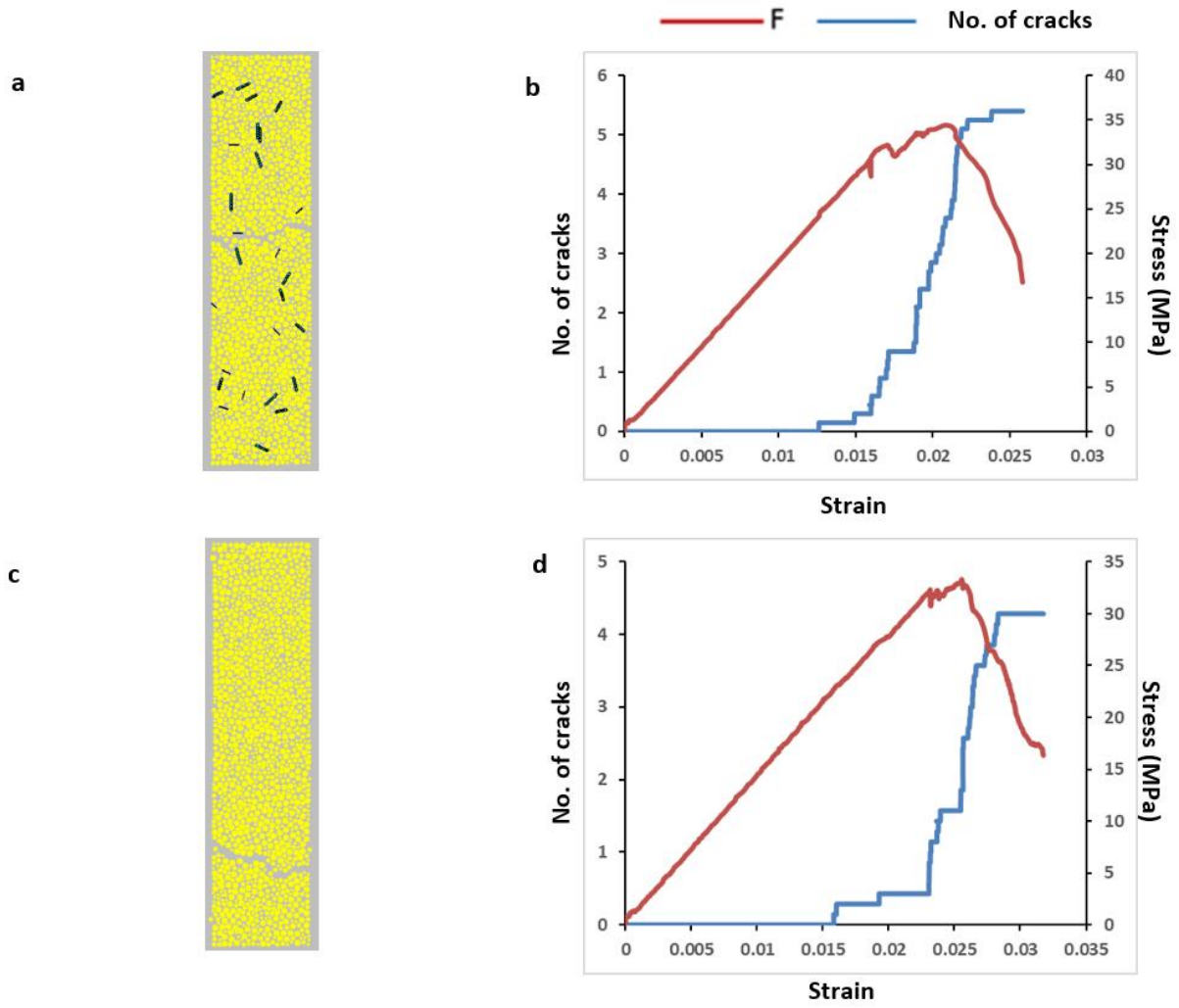

Figure 6.8 (a) Post-cracking crack pattern of SF-ECC; (b) Tensile stress/micro-crack number vs strain in SF-ECC; (c) Post-cracking crack pattern of CB-ECC and (d) Tensile stress/micro-crack number vs strain in CB-ECC.

6.2.2.2 Uniaxial tensile test

The post-cracking crack patterns with load, number of cracks and tensile stress in terms of strain from numerical simulation for the SF-ECC and CB-ECC plates are shown in Figure 6.8. In comparison of the simulated result of the stress-strain curve with that of the experimental result for SF-ECC, both curves show tensile strength around 5.5 MPa. The

failure strain and curve shape fit well to each other. The electrical measurement result is therefore included in Figures 6.9(c) and (d) with the crack number simulation domain by strain for comparison. As in the flexural test, the simulated crack density development and the resistance change in tensile testing also show similar variation trends. But at the state before the failure point of SF-ECC, even though the cracks were generated gradually, the resistance does not increase with the number of cracks. In contrast, the response of the resistance to changes in crack density shows better consistency in the CB-ECC. This may be caused by the existence of SF bridges at interfaces of the initial micro-cracks. Therefore, although the SF-ECC shows better conductivity, the CB-ECC shows higher self-sensing sensitivity for crack detection.

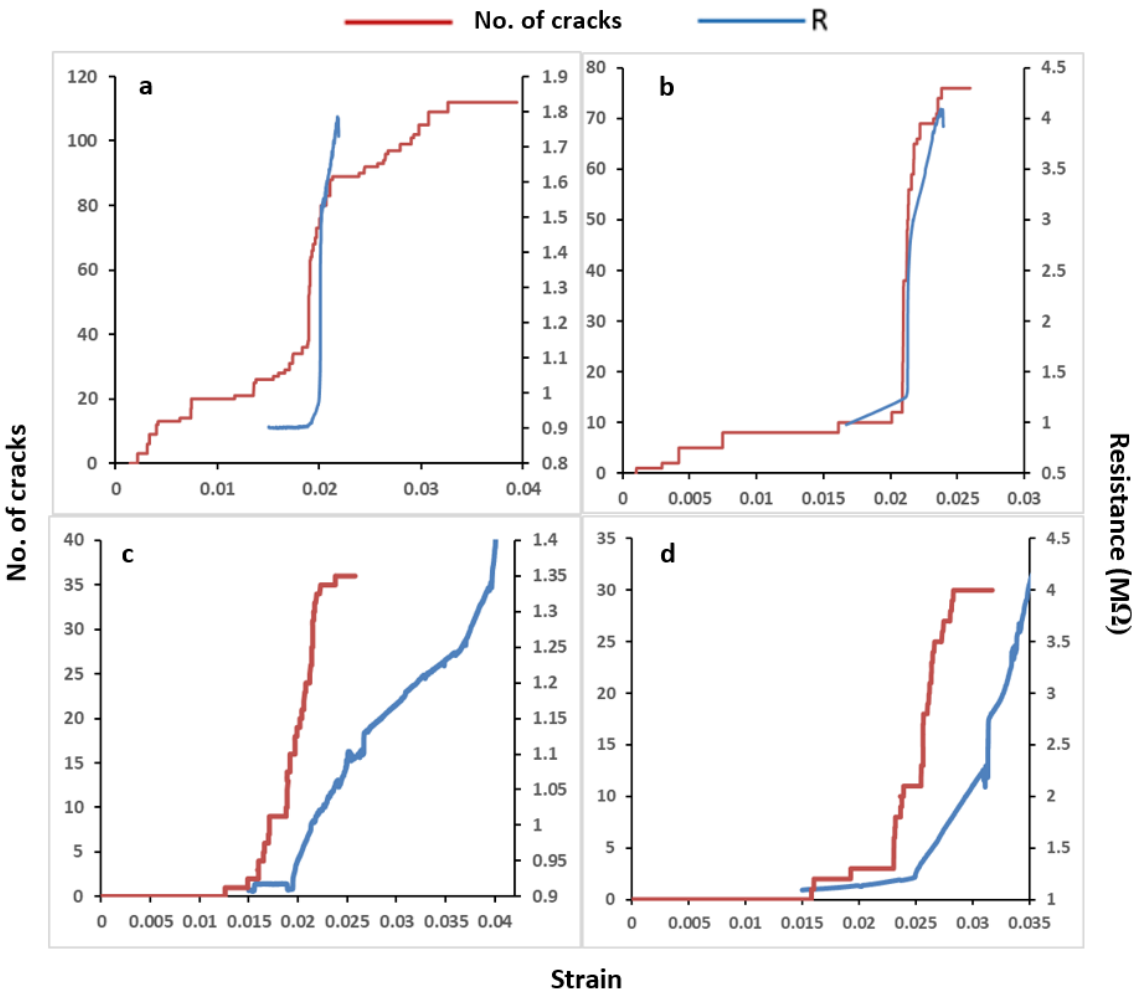

Figure 6.9 Resistance-strain curve and micro-crack number-strain curve for (a) SF-ECC in bending test; (b) CB-ECC in bending test; (c) SF-ECC in tensile test; (d) CB-ECC in tensile test.

6.3 Summary

In this chapter, the mechanical and electrical properties in terms of self-sensing capacity of two types of ECC, i.e. SF-ECC and CB-ECC, were investigated experimentally and by numerical simulation. It was observed that the use of SFs or CB powders enhanced the flexural strength, tensile strength and conductivity of the ECC materials. Steel fibres induced superior results in both mechanical and electrical performance, primarily due to

the bridging mechanism facilitated by the long bar shape of those fibres. From the experimental and numerical results, the ECC materials showed excellent self-sensing behaviour for crack detection, but CB-ECC demonstrated higher sensitivity than SF-ECC. The resistance change measured at the surface showed a similar trend as the crack developed. The findings of the different effects of SF and CB on the mechanical and electrical properties for the self-sensing performance of ECC materials provide useful information for future study of the sensitivity of the self-sensing capacity for micro-crack detection and optimisation of the design of ECCs.

Chapter 7 Crack Detection in ECCs by Using ERT

In the present chapter, a probabilistic diagnostic algorithm for ERT, which was introduced in Chapter 4, is proposed to detect cracking in ECC with the involvement of fewer measurements and simpler tomography reconstruction. The feasibility and accuracy of this method are studied using SF-PVA ECC specimens with a single edge crack, an additional crack in a specimen with existing crack, a single diagonal internal crack, and dual edge cracks, representing the most frequently occurring crack patterns. The proposed ERT method was also applied for detecting the crack propagation of SF-PVA ECC in tensile test.

7.1 ERT for artificial cracks

7.1.1 ERT measurements

Three SF-PVA ECC plate specimens with dimensions of 300 mm×50 mm×12 mm were cast for ERT measurement with different crack layouts, following the preparation process in Chapter 4. The monitoring area of the specimen was a rectangular area of 56 mm×42 mm in the middle. 28 copper electrodes were bonded on same face of the specimen as a rectangular network with intervals of 7 mm. Forming the electrical conductive pathways by selected pairs of the electrodes, there were 26 conductive pathways in the oblique direction, 7 pathways in the vertical direction and 5 pathways in the horizontal direction, as shown in Figure 7.1. For each pathway, the measurement of electrical resistance was conducted before and after crack cutting, to obtain the change in resistance.

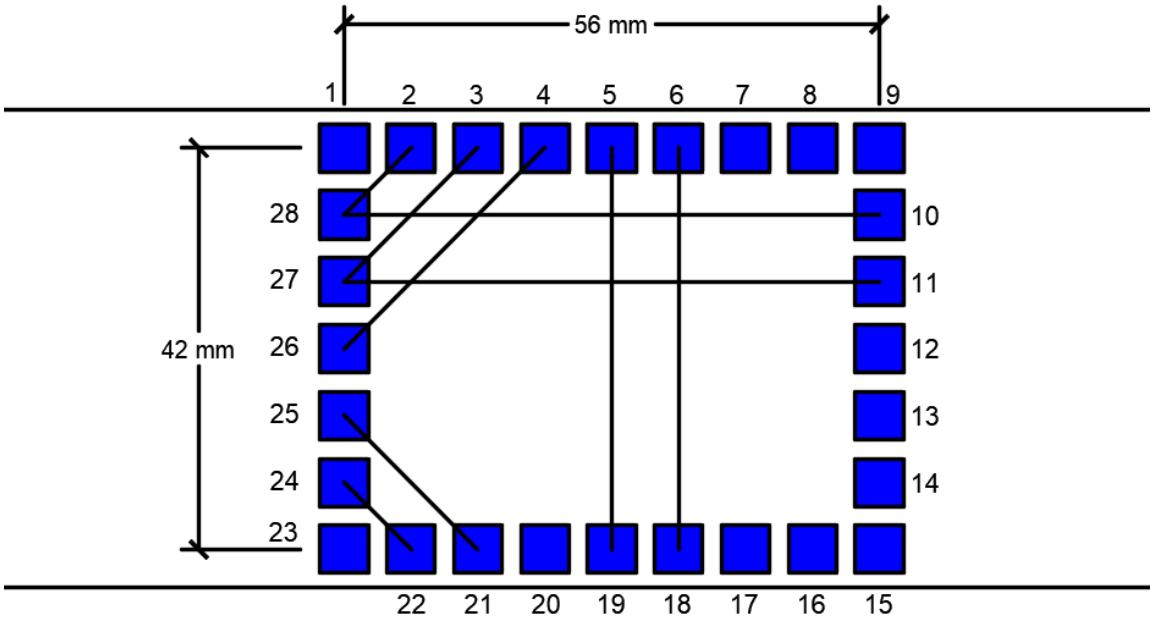

Figure 7.1 Typical electrode and conductive pathway layout. Black lines indicate examples of horizontal, vertical and oblique conductive pathways.

To measure the conductivity of cement-based materials, two main traditional techniques were used, which can be referred to as the two-point method and the four-point method according to the setup of the electrical probes, where both DC and AC can be used for each method. The DC method has certain drawbacks such as contact impedance and electrical polarisation, which induce a time-dependent reduction in conductivity during measurement [18]. In contrast, such effects do not have time to develop in the AC method when it is at a proper frequency. Therefore, the two-point or four-point AC method is the most feasible approach for electrical measurement of cementitious materials [15, 18].

Four through-thickness crack scenarios introduced by a 0.6 mm blade were investigated in this study to check the feasibility and accuracy of the proposed ERT method as applied to different crack patterns. The first scenario was a side crack produced by cutting a crack at

the edge of the plate specimen as shown in Figure 7.2(a), where the crack is marked by a red line. This type of crack usually occurs at a structure surface subjected to a force exceeding its tensile strength. In order to study the sensitivity of the current electrode layout with an interval of 7 mm for crack size, the initial crack length was cut as 3 mm, then extended to 5 mm, 7 mm and 14 mm, which covered crack sizes from around half of the electrode interval to twice the interval. The second scenario was designed to detect a newly generated crack on the specimen with an existing edge crack (Figure 7.2(b)). This would prove the feasibility of the proposed ERT method to detect an additional crack in aged structures with an existing defect. For this purpose, a 14 mm length crack was first cut on one edge of the specimen (marked as a grey dashed line) with the resistance measured as a benchmark. Another 14 mm length crack was then cut on the opposite edge and the corresponding resistance of each conductive pathway was measured again. The third scenario was designed to identify an internal diagonal crack, which simulated shear failure. The cut crack was 14 mm in length (Figure 7.2(c)) and was subsequently extended to 21 mm to visualise the difference in shape and intensity of the ERT images. The fourth scenario was used to study the feasibility of this ERT method for dual cracks: two 7 mm cracks were cut at two opposite edges of the specimen, as shown in Figure 7.2(d).

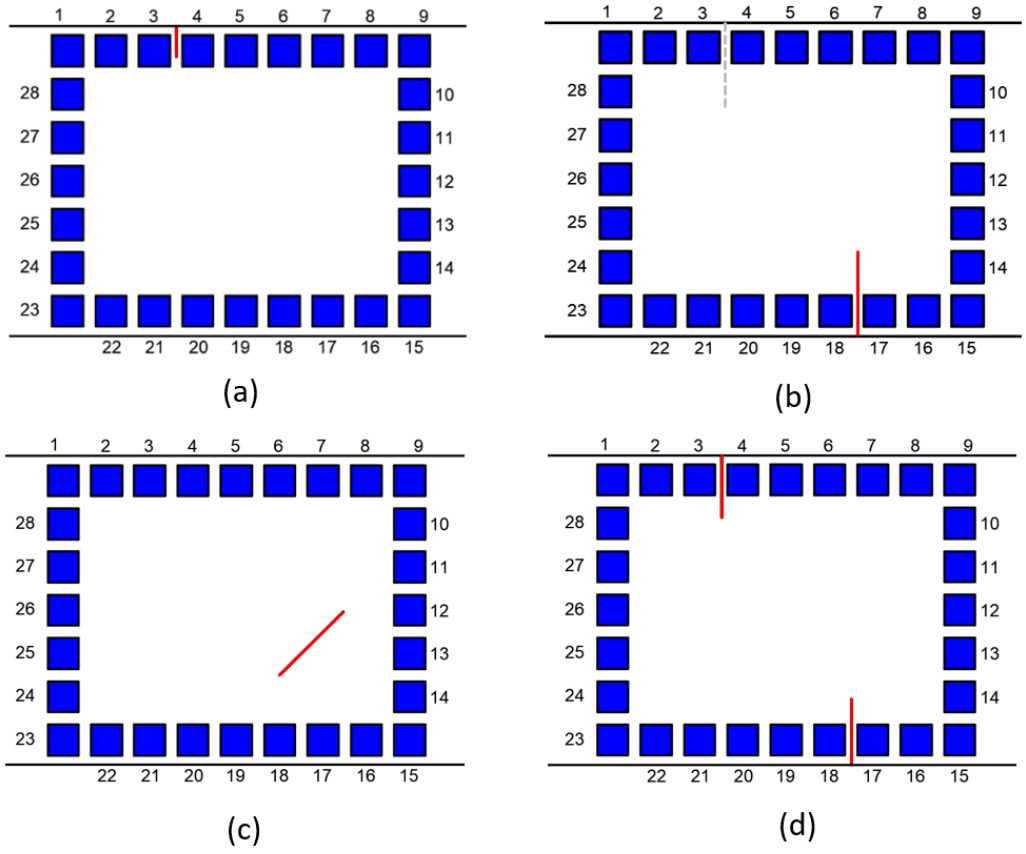

Figure 7.2 Crack location of (a) edge crack; (b) additional crack in specimen with existing crack; (c) internal diagonal crack, and (d) dual edge cracks.

7.1.2 Results and discussion

7.1.2.1 Identification of single edge crack

For the tomography calculation, the monitoring area was meshed into 100×100 uniformly distributed grids with the vertical interval of 0.42 mm and horizontal interval of 0.56 mm. The weight for each of these 10000 points was calculated with reference to all 38 conductive pathways. As mentioned, the scaling parameter was set as 0.05, which was determined by trial and error as the most feasible value for such a grid size in this study.

The tomograms reconstructed using the proposed ERT algorithm for four side cracks are shown in Figure 7.3, where the actual crack locations are marked as black lines.

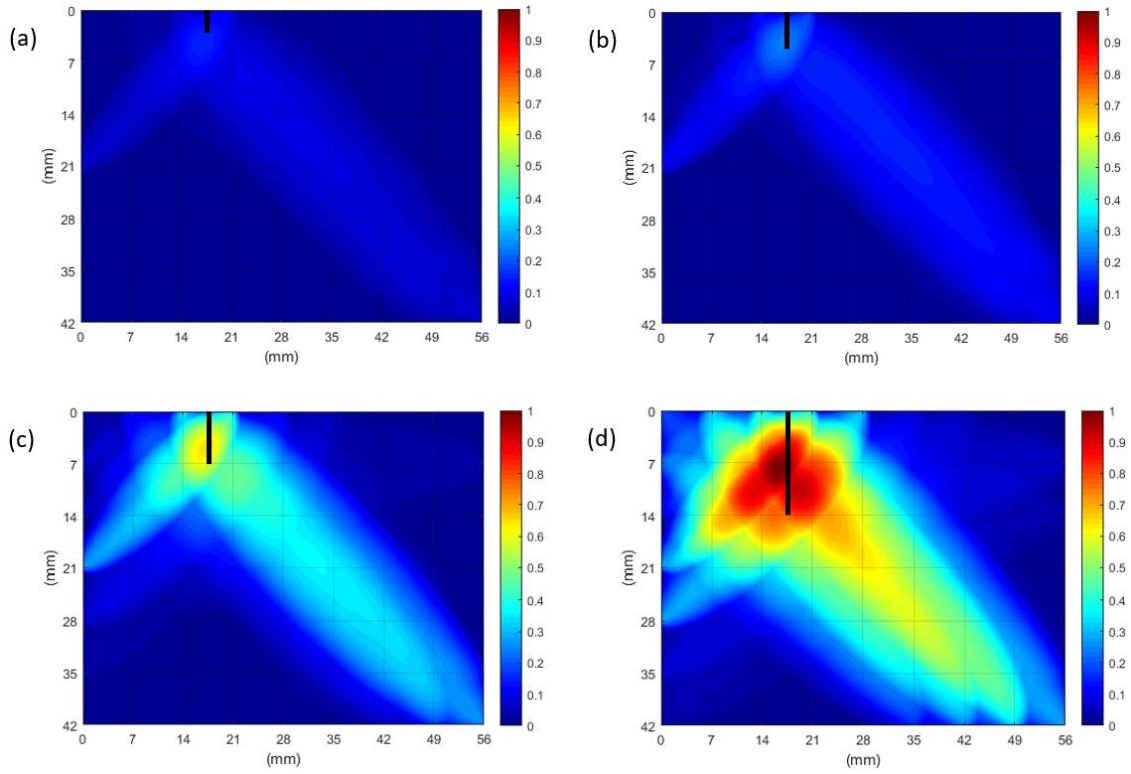

Figure 7.3 ERT tomograms for single edge crack of (a) 3 mm length; (b) 5 mm length; (c) 7 mm length; and (d) 14 mm length.

To compare the intensity of tomograms of different crack lengths, the scaling range of the colour bar was normalised by the value for the most intensive point from the scenario with a 14 mm crack. It can be observed that the predicted crack location for each case is accurately identified at the left of the top edge. With the crack size increasing from 3 mm to 14 mm, the affected area in the image is enlarged as well as having increasing colour intensity which indicates the increase in damage severity. On the other hand, it can be observed that the size predicted for the 3 mm crack is greater than the actual size and quite

similar to that of the 5 mm crack, an effect that may mainly be caused by the greater interval between the electrodes (7 mm in this study). It was therefore deduced that the resolution necessary for correctly estimating crack size was about half of the electrode interval.

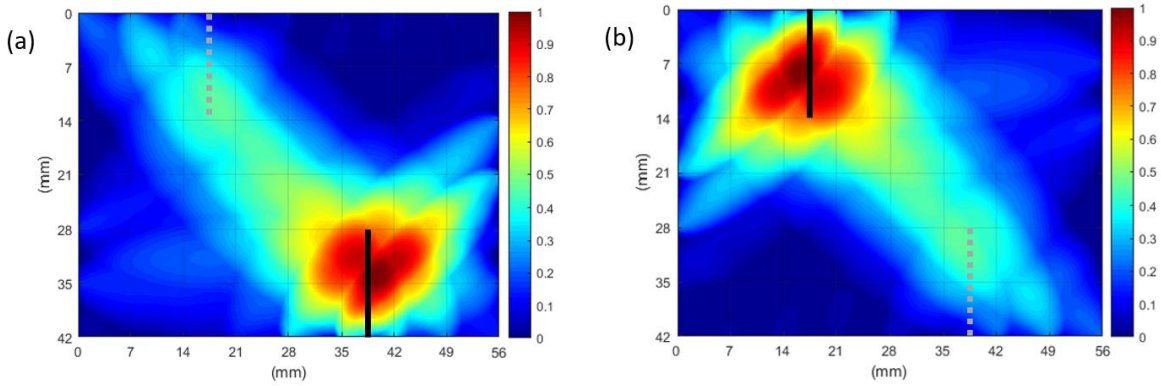

Figure 7.4 Prediction of additional edge crack (a) ERT tomogram; (b) 180˚ rotated ERT tomogram for additional single edge crack of 14 mm.

7.1.2.2 Identification of additional crack in specimen with crack

The ERT tomogram for an additional crack where the specimen from scenario 1 with one edge crack as existing damage was measured as the benchmark is shown in Figure 7.4(a). It is evident that the new crack at the lower right is well located and the previously existing crack at the top left does not cause any disturbance to the detection of the new introduced crack. Since the new crack location is centrosymmetric with that in single edge crack scenario, an 180˚ rotated tomogram is presented in Figure 7.4(b) for comparison with that for the 14 mm single edge crack (Figure 7.3(d)). It is observed that the patterns of the ERT tomograms are quite similar. In particular, the intensity of the predicted critical area is quite similar for these two scenarios, where the highest possibility of the presence of the crack in this ERT tomogram is 0.9384 compared with that for the scenario of the 14 mm single

edge crack. It is therefore verified that the proposed ERT method shows good feasibility for ageing structures in terms of new crack localisation and severity assessment.

7.1.2.3 Identification of internal diagonal crack

To simulate cracks induced by shear force, two diagonal cracks at 45° to the horizontal direction were cut, first as 14 mm and then extended to 21 mm at the lower right corner of the second specimen. The corresponding ERT tomograms are shown in Figure 7.5, with marked actual crack locations, which are accurately covered by the predicted crack area. Once the upper limit of colour bars is unified by the maximum value in the tomogram for the 21 mm crack, the area predicted for the 14 mm crack is noticeably smaller. Since the direction of the crack was not clear, a simple false-colour filtering process, which could reduce the noise by measurement and improve the focus on the critical area, was used to highlight the location and size of the crack in the tomogram [83]. This was accomplished by setting a proper threshold for the value of the cumulative weighted change. As shown in Figure 7.6, after adjustment of the scale of the colour bar, the direction of the highlighted critical area is well aligned with 45°, which is the actual direction of the crack, demonstrating the good prediction capability for damage direction by this ERT algorithm.

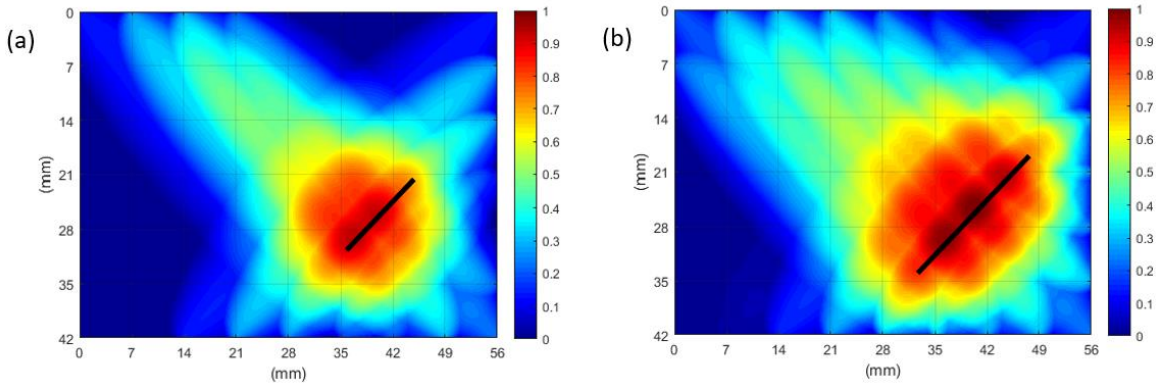

Figure 7.5 Adjusted ERT tomograms for internal diagonal crack of (a) 14 mm length; and (b) 21 mm length.

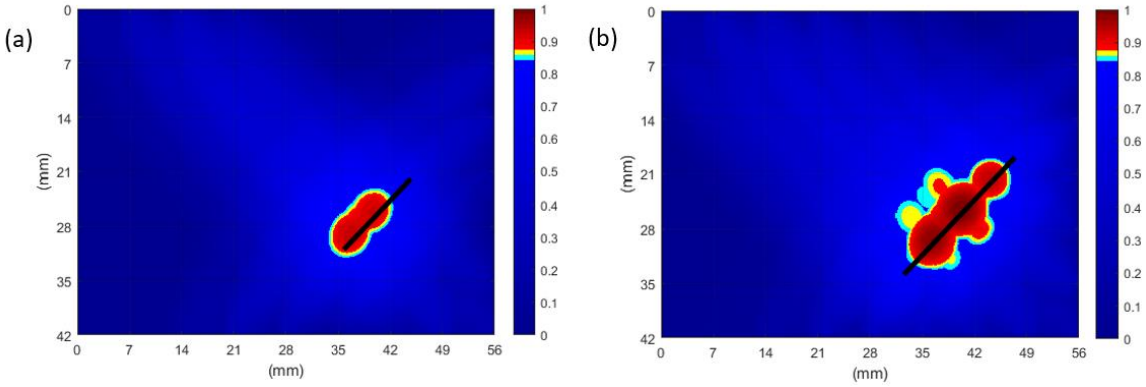

Figure 7.6 Adjusted ERT tomograms for internal diagonal crack of (a) 14 mm length; and (b) 21 mm length.

7.1.2.4 Identification of dual edge cracks

In practice, there may be more than one major crack in a cementitious structure. Thus, the feasibility of the proposed ERT method for dual cracks is verified in this section. Two individual 7 mm cracks were made at the top left and bottom right edges of the third specimen. The reconstructed ERT tomogram is shown in Figure 7.7(a), where the critical damage area is predicted as a long diagonal crack, whereas the two actual cracks should be

located individually at the two ends of this predicted crack. The main reason for this phenomenon is the different contributions of conductive pathways that suffer a marked change in electrical resistance when the ERT is constructed. Table 7.1 lists the ten conductive pathways with the greatest change in resistance measurement. It is observed that the greatest change in electrical resistance, indicating the highest probability of the presence of crack, occurs on the conductive pathway 2-16 that passes through both cracks, as shown in Figure 7.8(a). As a result, the contribution of pathway 2-16 is inappropriately highlighted in the final ERT image.

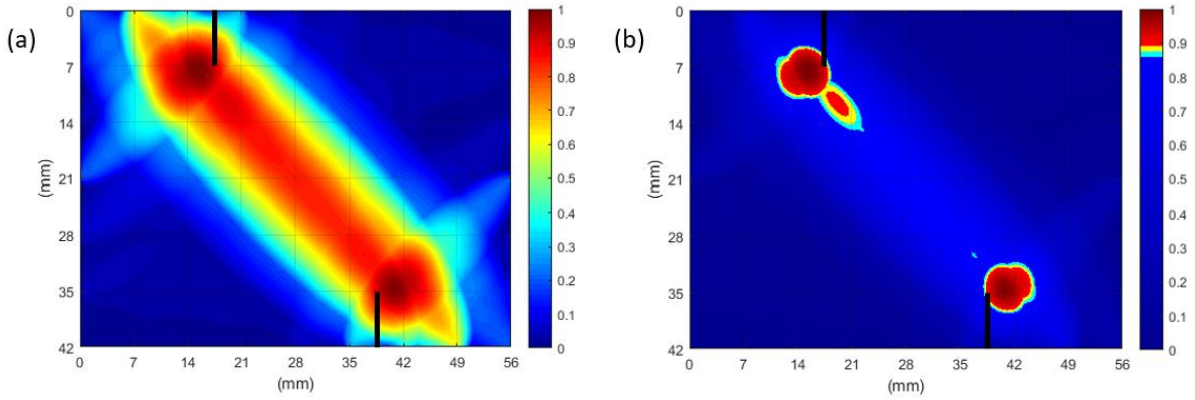

Figure 7.7 Prediction of dual crack (a) ERT tomogram; (b) adjusted ERT tomogram for dual edge cracks of 7 mm length.

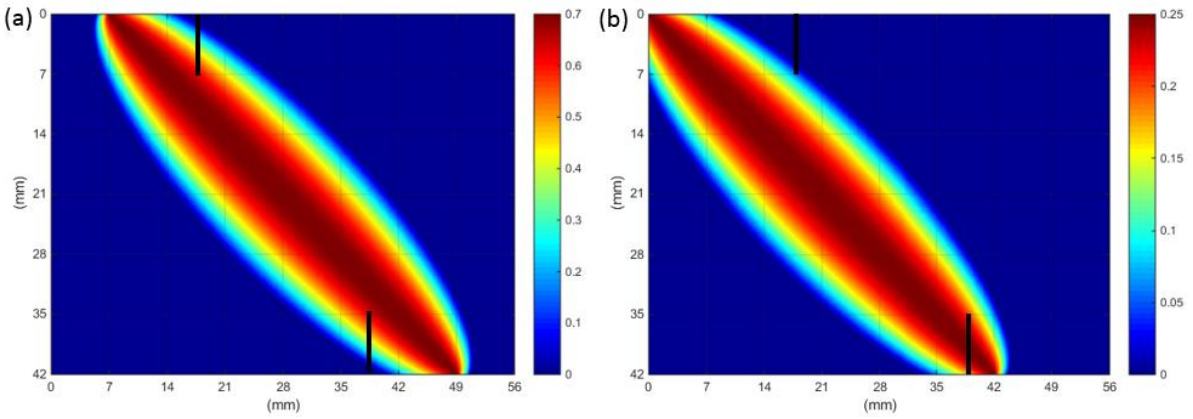

Figure 7.8 Influence area of conductive pathway that (a) passes through both cracks; (b) passes through one crack and is close to the other crack.

To eliminate this incorrect prediction, the scale of the colour bar was adjusted as shown in Figure 7.7(b), where two separate damage areas are clearly highlighted, which, however, show lower accuracy than the scenario of the single crack. This effect may result from the contribution of certain conductive pathways which pass through one of the cracks while being a short distance from another crack. For example, conductive pathway 1-17 (Figure 7.8(b)) passes precisely through the bottom crack, with the higher probability of the presence of crack in this pathway, which however generates another significant influence area to the left of the top crack. As a result, the cumulative weighted change of resistance around the top crack shifts left and downward as shown in Figure 7.7(b), unavoidably compromising the precision of the proposed method for dual crack identification.

Table 7.1 Electrical measurements for specimen with dual edge cracks

Position*	R_0 (MΩ)	R (MΩ)
2-16	1.759	2.991
1-17	1.832	2.290
3-15	1.717	2.146
12-18	1.479	1.864
4-26	1.449	1.811
14-24	1.804	1.840
7-11	1.607	1.639
5-25	1.668	1.785
11-19	1.823	1.914
3-27	1.717	1.802

*Note: Position gives the starting and ending electrode numbers of the conductive pathway in Figure 7.1.

7.2 ERT for uniaxial tensile test

7.2.1 ERT measurements

SF-PVA ECC Plate specimens with dimensions of 300 mm×50 mm×12 mm were prepared for uniaxial tensile test, synchronising electrical resistance measurement for ERT tomogram construction. Considering the uncertainty of the initiate crack location for tensile

test, the monitoring area of the specimen was extended twice than that designed in artificial crack detection. Therefore, a rectangular monitoring area of 112 mm×42 mm was set in the middle of each specimen during the tensile test. 28 copper electrodes were attached on the same face of the specimen as a rectangular network with intervals of 7 mm in the width direction and 14 mm in the length direction. Forming the electrical conductive pathways by selected pairs of the electrodes, i.e. 26 conductive pathways in the oblique direction, 7 pathways in the vertical direction and 5 pathways in the horizontal direction. Silver conductive paste was used to improve the contact strength with minimum impact to resistance measurement. The preliminary preparation of specimen before loading test is shown in Figure 7.9(a).

The experimental setup for the uniaxial tensile test is shown in Figure7.9(b). Thin aluminium plates (50 mm×50 mm) were bonded to the ends of the specimens by epoxy (ARALDITE® 420 A/B) to avoid stress concentration at the grip surface. The tests were conducted on the Baldwin 500 kN testing machine with displacement control. Since there is no specific standard for uniaxial tensile testing of cementitious materials, the recommended displacement rate of 0.5 mm/min has been used [15].

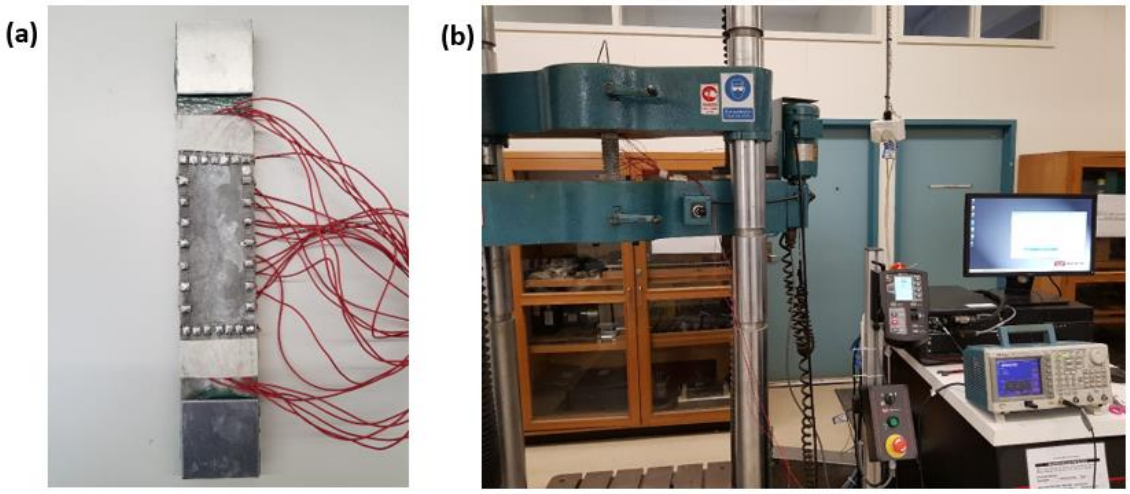

Figure 7.9 (a) Prepared specimen for tensile test; (b) Experiment set up for tensile test synchronising ERT measurement.

The ERT measurement scenario is to record the resistance at different cracking stages to construct the relevant ERT tomograms. Then the acquired tomograms will be compared with each other to judge the feasibility as well as sensitivity of the proposed ERT algorithm for practical crack detection. According to the conclusion in Chapter 6 that the resistance change measured at the surface showed a similar trend as the crack developed for SF-PVA ECC, the resistance of selected pair of electrodes will be continuously measured during the tensile test. Once there is a sudden increment in the resistance of the specific pair of electrodes, the load of the test machine will be hold. A whole set of the ERT measurement will be conducted to all the conductive path ways. Due to the unpredictability of the initial crack starting point, three pairs of electrodes have been selected and measured (Figure 7.10), which are pair 28-10 for the condition that crack initiates on top edge, pair 26-12 for the condition that crack initiates in the middle and pair 24-14 for the condition that crack initiates at the bottom edge. To achieve the measurement scenario, three Agilent 34461A

multimeters were set as AC meters to calibrate the current trend in parallel, sharing one constant voltage source with 5 kHz frequency and ±5 V amplitude from the signal generator. The ERT measurement will be conducted three times during the whole tensile test for each specimen.

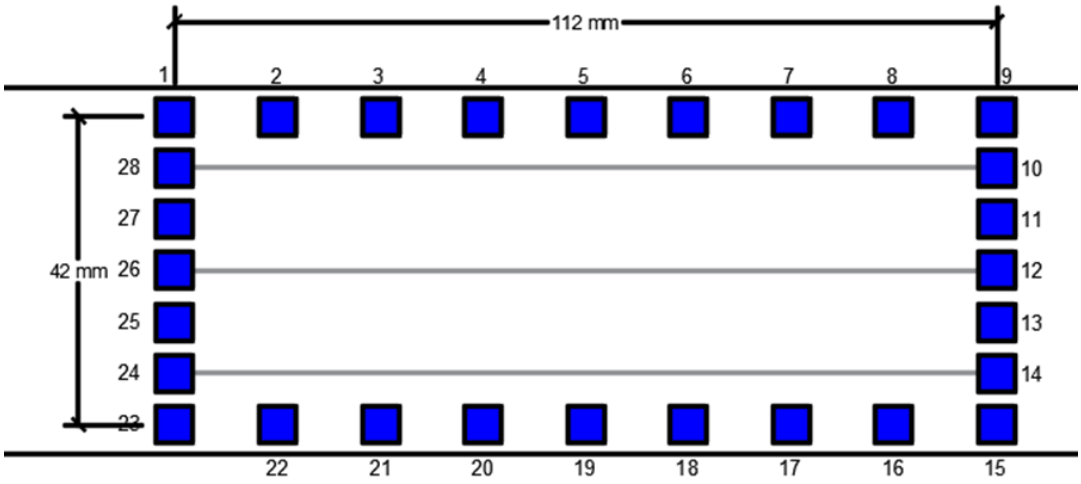

Figure 7.10 Electrode layout and three selected conductive path ways.

7.2.2 Results and discussion

After several tests and ERT image construction, the cracking development can be concluded into three typical types: crack within the monitoring area, crack exceeding the monitoring area and crack out of monitoring area. Since nothing can be detected while the crack propagates outside the measurement range, only the first two conditions are discussed here.

7.2.2.1 Crack within monitoring area

In this scenario, the major crack will initiate from one longitudinal edge to the other longitudinal edge and propagates inside the measurement area. The tensile stress strain curve of one specimen with resistance strain curve of the three selected conductive path ways are shown in Figure 7.11. The specimen has tensile strength at 5.97 MPa, and tensile strain around 2.69%. In the graph, lane 1 represents conductive path way from electrode 28 to 10; lane 2 is for conductive path way from electrode 26 to 12 and lane 3 is measurement result for electrode pair 24-14. The timing to apply the ERT measurement for all pairs of electrodes is when there is an obvious increment in any of the three resistance curves, i.e. the measured AC trend on the multimeter. The first ERT measurement was conducted when the strain reached about 2.48%. At that time the lane 1 and lane 2 turned to increase (the measured current started to decrease). From visual observation, there was no clear crack on the surface of the specimen. The second ERT measurement was conducted when strain grew to 2.88%. Major crack started from top edge and extended to the other side soon. In the meantime, the resistance of lane 3 turned to increase. Lastly, the final measurement of ERT was done within a roughly similar time interval between the previous two, due to the steady increasing rate for all three resistance strain curves. The strain for that was about 3.2%, and the specimen was going to break into two segments.

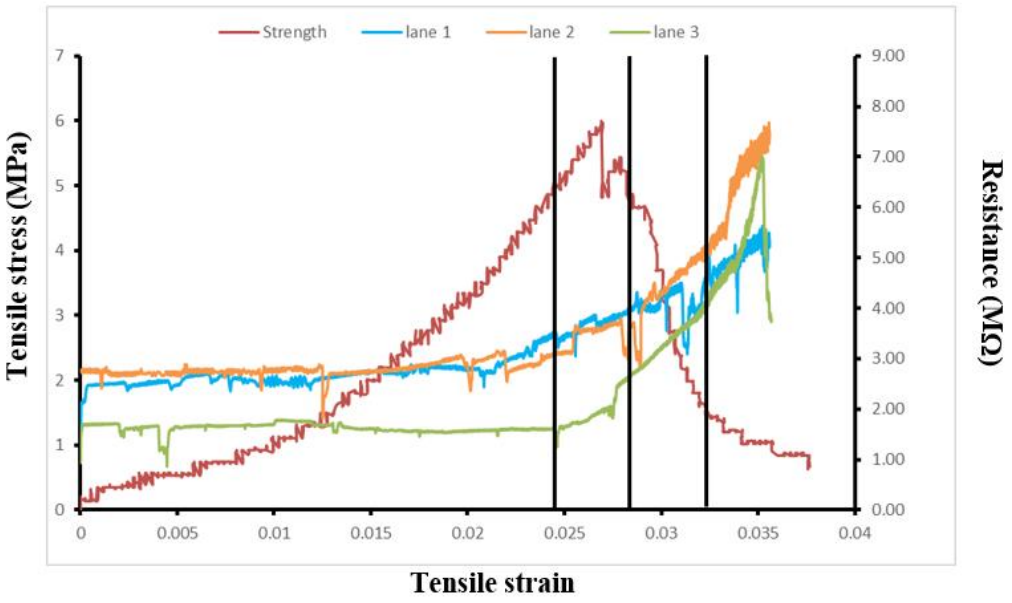

Figure 7.11 Stress strain curve of specimen and resistance strain curve of three selected conductive path ways for specimen with crack inside the monitoring area.

The ERT tomograms of the specimen constructed based on the three ERT measurements are given in Figure 7.12. The colour bar on the right is the probability level for the existence of the potential cracks. To get a better comparison, the maximum values of the colour bars were set as the same as the maximum value for the most intense value by the third measurement, by which all of values are normalised. From the ERT image for first measurement, it is shown that some internal cracks or very narrow cracks may be generated closed to the top edge of the specimen, while no visual crack can be seen at that time. And indeed, the construction of the first measurement is mainly due to the earliest change of resistance in lanes 1 and 2, which are nearby to top edges. The intensity of colour is getting stronger from the first to the last image. The potential cracking area propagates from top to bottom accordingly, which is the same as observed in the test. Therefore, the feasibility of the ERT method has been proved for real time crack development monitoring in

practical tensile test. The method can detect not only the location, but also the intensity of the crack.

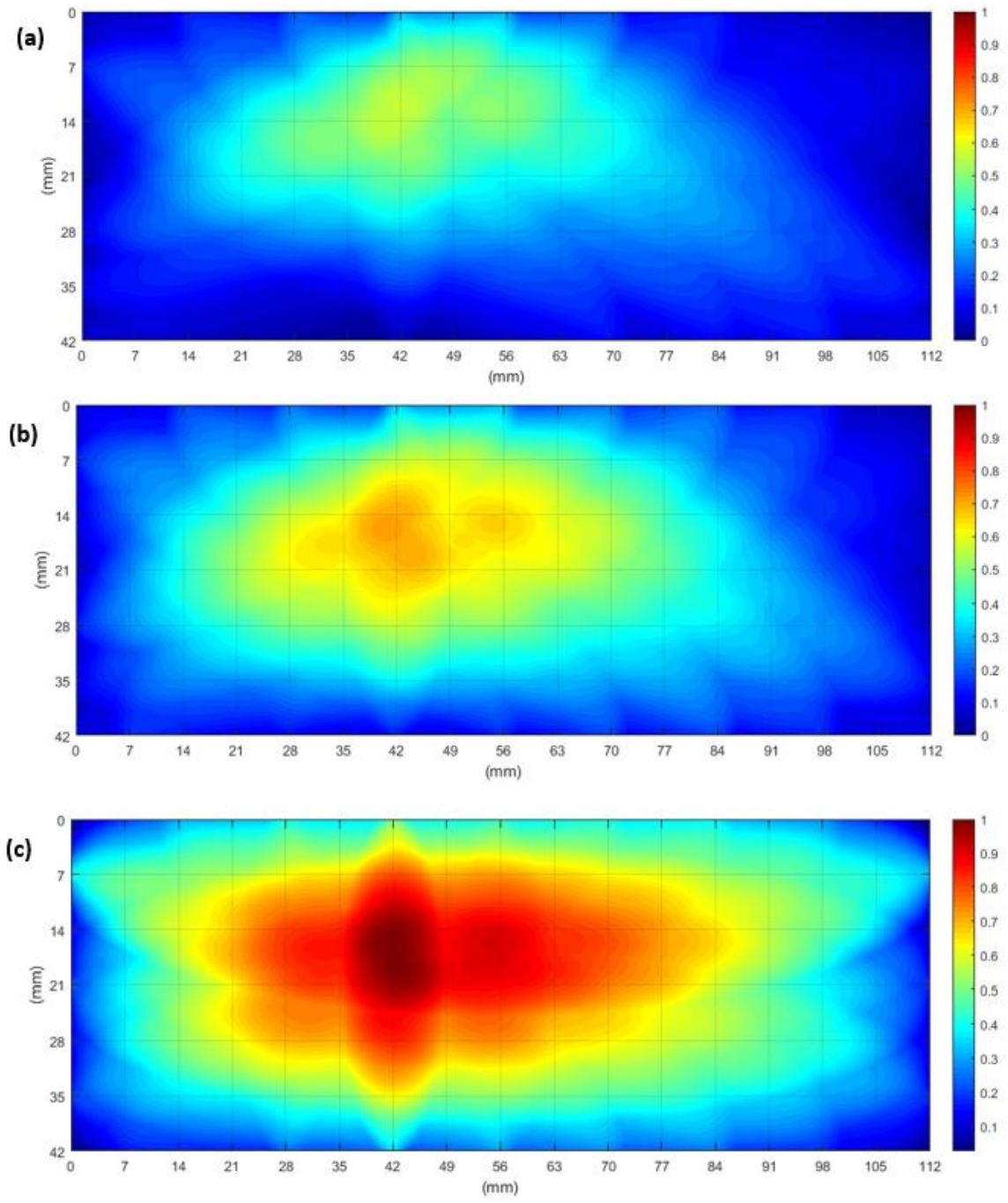

Figure 7.12 ERT tomograms for specimen with crack inside the monitoring area when the tensile strain is of (a) 2.48%; (b) 2.88% and (c) 3.2%.

7.2.2.2 Crack exceeding monitoring area

In certain scenarios, the crack initiates in the monitoring areas but later propagates out of the monitoring area partly, as shown in Figure 7.13. The crack initiated at the bottom edge (on the left in the figure) of the specimen and grew in a diagonal direction and propagated out of the monitoring area on the left side (on top in the figure).

Figure 7.13 Crack pattern for crack exceeds monitoring area in tensile test.

In this case, the tensile stress strain curve of one specimen with resistance strain curve of the three selected conductive path ways are shown in Figure 7.14. The specimen is of tensile strength at 5.51 MPa, and tensile strain about 2.45%. The first ERT measurement was taken when the strain was about 2.11%, since the resistance strain curve of lane 3 began to increase dramatically. The second ERT measurement was conducted when strain reached 2.78%, which is also because of the increment in the curve of lane 3. The last measurement was at strain about 3.43%. At that time the resistance strain curve for lane 2

starts to increase but that for lane 1 still shows marginal change. Observing the electrode layout in Figure 7.10 and crack pattern in Figure 7.13, it is noticed that the crack crossed lane 3 first and then cut the end of lane 2 just before it exceeded the monitoring area. As a result, it did not go through lane 1, therefore with least impact on the resistance measurement of it. These facts are all clearly shown in the measured resistance strain curve.

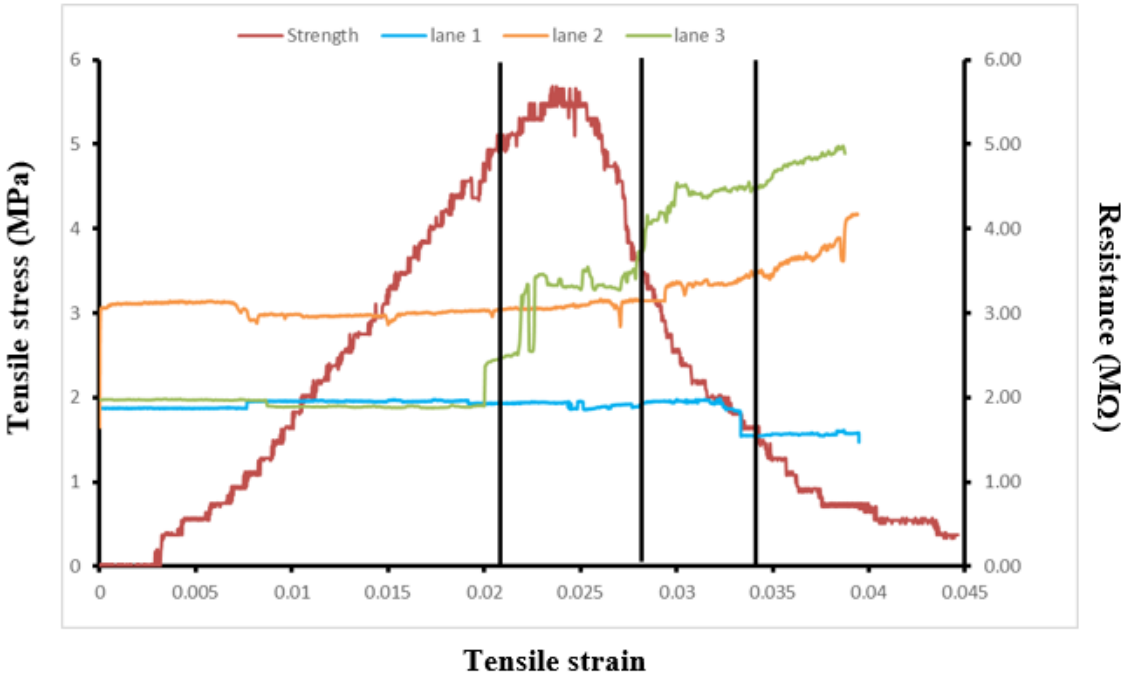

Figure 7.14 Stress strain curve of specimen and resistance strain curve of three selected conductive path ways for specimen with crack exceeding the monitoring area.

Three ERT tomograms are presented in Figure 7.15, where the images show the crack location and orientation in good resolution. The first one shows the least intensity, since the crack was just starting to extend at the left bottom corner. The pattern and intensity for the next two ERTs are almost the same. This is because the crack that develops outside the

monitoring range would have minimal impact on the detection result that is based on the data from monitoring area.

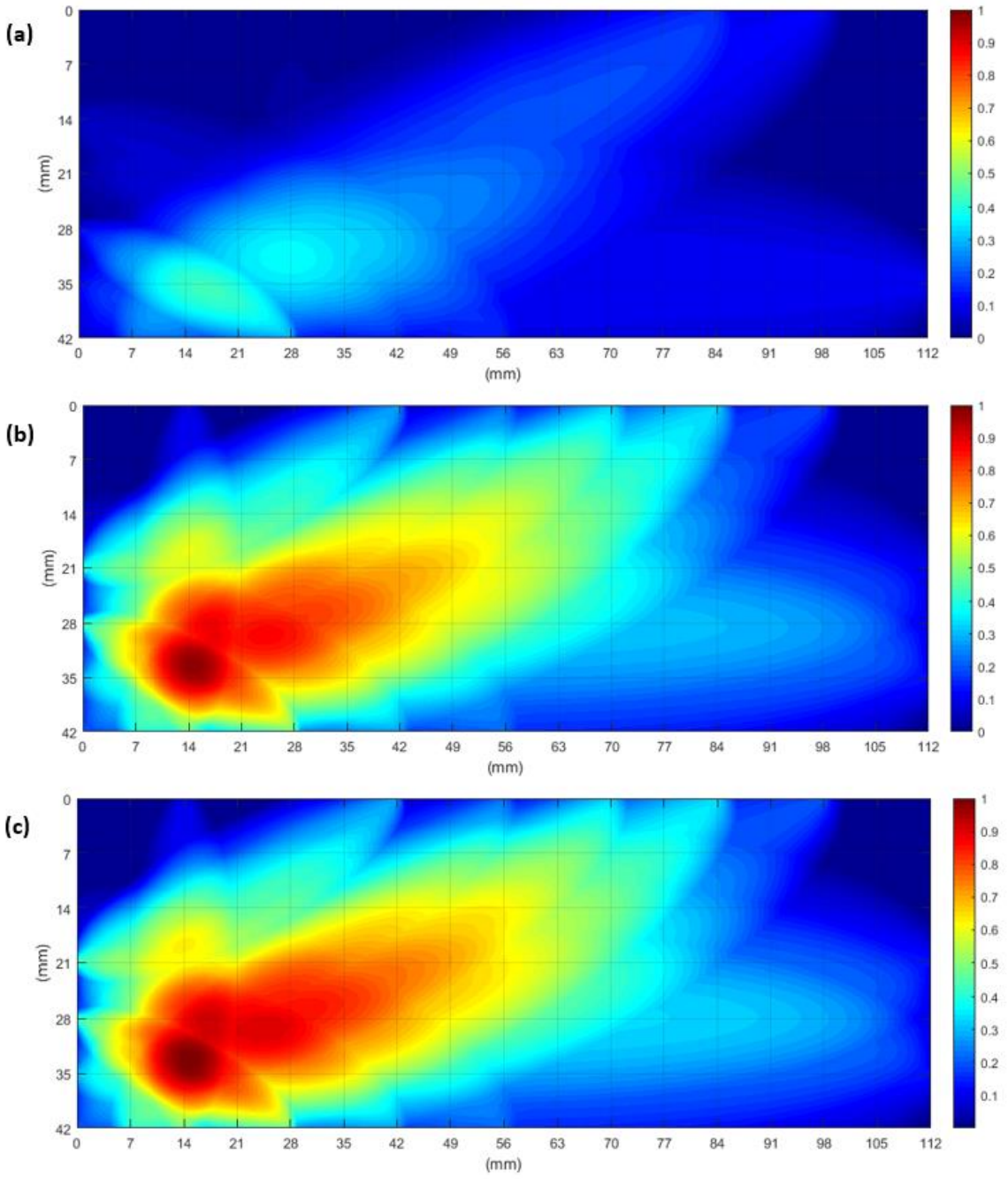

Figure 7.15 ERT tomograms for specimen with crack exceeding the monitoring area when the tensile strain is of (a) 2.11%; (b) 2.78% and (c) 3.43%.

7.3 Summary

In this chapter, a new ERT method based on a probabilistic diagnostic algorithm was developed for crack detection of ECCs fabricated with PVA fibres and steel fibres. Specimens with different crack patterns were prepared and the electrical resistance was measured to construct relevant ERT tomograms. The feasibility and accuracy of the proposed ERT method for identification of different crack cases were studied and discussed.

It was observed that the proposed ERT method is able to detect and quantify a single edge crack and an internal diagonal crack. In the resolution study, it was shown that the minimum size of the crack that could be identified by the proposed method was around half of the inter-electrode interval. It was also proved that this ERT method could be applied for ageing structures, where the tomogram could present the location and severity of an additional crack and was not influenced by an already existing crack. For the dual crack scenario, the feasibility of this method was also acceptable. Nevertheless, because of the effect of the different influence areas of certain conductive pathways which were close to both cracks, the resulting accuracy was not as good as that for single crack cases. The proposed ERT method was then proved feasible for crack location and development detection in practical tensile tests for different cracking conditions, e.g. crack within the monitoring area and crack exceeding the monitoring area. It is expected that the proposed method can provide a sound and convenient method for in-situ damage detection and structural health monitoring of ECCs.

Chapter 8 Conclusions and Recommendations for Future Study

8.1 Main findings of this thesis

The aim of the work presented in this thesis was to develop and optimise the self-sensing property of ECCs supported by innovative technologies, e.g. DEM and ANN. These approaches helped to provide a comprehensive understanding of electrical property of ECCs and to redesign the composition of ECC and optimise both mechanical properties and self-sensing properties. The proposed strategy is also to use the self-sensing behaviour of ECC to detect microcrack at the early stage. A new ERT method was applied to detect and characterise the damage development in ECC.

To accomplish these targets, the following research studies were carried out.

In Chapter 2, the development of ECC is introduced. The characteristics of ECC are studied by reviewing different types of ECC with various material composition. The deeper understanding of failure mechanism of ECC will help the studies in the following chapters regarding the design and optimisation of ECC properties.

The electrical resistance measurement methods for cementitious materials were introduced and compared in Chapter 3 for resistance measurement method test and selection. The self-sensing studies of ECC were reviewed and summarised, finding that previous studies still have not covered the influence of microcracking to the sensitivity of conductive capacity of ECC, which is relevant to the inherent mechanism of ECC and would contribute to the

design of ECC. Commonly used ERT methods and studies relevant to cementitious materials are illustrated, which provides a comprehensive understanding of ERT.

Chapter 4 shows the ECC specimen preparation process and electrical resistance measurement method applied for the proposed studies. Both DC and AC methods have been tested to ECC specimen. The principle of ANN was introduced to provide a gateway for ECC design and optimisation. DEM models and simulation process were reviewed for the proposed cracking study of ECC. An innovative ERT method based on a probabilistic diagnostic algorithm has been presented and proved feasible for ECC by some preliminary experiments.

Prediction of mechanical and electrical properties of ECCs was developed by the ANN technique in Chapter 5. ANN models for PVA-ECC and SF-ECC were trained and validated based on collected data from existing researches. Series of experimental tests were conducted to assess the capability of the well-trained ANN models. The small differences between the predictions and tested values indicated that estimation of the mechanical and electrical properties of ECCs using ANNs could be achieved with good accuracy, benefiting the ECC design with good mechanical properties as well as proper electrical properties, which can be used in the following self-sensing studies in Chapter 6 and 7.

In Chapter 6, the mechanical and electrical properties in terms of self-sensing capacity of two types of ECC, i.e. SF-ECC and CB-ECC, were investigated experimentally and by numerical simulation. It was observed that the use of SF or CB powders enhanced the flexural strength, tensile strength and conductivity of the ECC materials. Steel fibres

induced superior results in both mechanical and electrical performance, primarily due to the bridging mechanism facilitated by the long bar shape of those fibres. From the experimental and numerical results, the ECC materials showed excellent self-sensing behaviour for crack detection, but CB-ECC demonstrated higher sensitivity than SF-ECC. The resistance change measured at the surface showed a similar trend as the crack developed. The findings of the different effects of SF and CB on the mechanical and electrical properties for the self-sensing performance of ECC materials provide useful information for the study of the sensitivity of the self-sensing capacity for micro-crack detection and optimisation of the design of ECCs.

In Chapter 7, a new ERT method based on a probabilistic diagnostic algorithm was developed for crack detection of ECCs fabricated with PVA fibres and SF. Specimens with different crack patterns were prepared and the electrical resistance was measured to construct relevant ERT tomograms. The feasibility and accuracy of the proposed ERT method for identification of different crack cases were studied and discussed. It was observed that the proposed ERT method is able to detect and quantify a single edge crack and an internal diagonal crack. In the resolution study, it was shown that the minimum size of the crack that could be identified by the proposed method was around half of the inter-electrode interval. It was also proved that this ERT method could be applied for ageing structures. For the dual crack scenario, the feasibility of this method was also acceptable. The proposed ERT method was then proved feasible for crack location and development detection for different cracking conditions e.g. crack within the monitoring area and crack exceeding the monitoring area.

8.2 Future work

- For ECC optimisation design by ANN, larger data sets need to be collected or created for the ANN model training to achieve a more accurate and robust model.
- A variety of commonly used constituents as different inputs should be employed into the ANN model. For instance, different types of superplasticizer and different batches of class F fly ash that may result in different mechanical properties of ECCs can also be included for training.
- The quantitative analytical relationships between the damage development, damage tolerance and resistance change of different types of ECC are worthy of investigation.
- Some microscope observation techniques can be used to predict and observe the microcracking behaviour of ECC, comparing with the monitoring results by self-sensing studies.
- The ERT method used in this study should be validated in more types of loading tests against various damage patterns, such as compressive test and four-point bending test. Some influence factors in common circumstances need to be taken into consideration, such as temperature and humidity. Relevant correlation function or method need to be studied, to make this technique to be widely applied in practice.

References

1. *"Elliot Lake mall roof collapse: Coroner investigating deaths of two women"*, in *Toronto Star*. 2012.
2. *"Italy bridge: Dozens feared dead in Genoa as motorway collapses"*, in *BBC News*. 2018.
3. McCann, D. and M. Forde, *Review of NDT methods in the assessment of concrete and masonry structures.* NDT & E International, 2001. **34**(2): p. 71-84.
4. Rehman, S.K.U., et al., *Nondestructive test methods for concrete bridges: A review.* Construction and Building Materials, 2016. **107**: p. 58-86.
5. Li, Z., *Nondestructive Testing in Concrete Engineering*, in *Advanced Concrete Technology*. 2011, John Wiley & Sons, Inc. p. 381-475.
6. Han, B., S. Ding, and X. Yu, *Intrinsic self-sensing concrete and structures: A review.* Measurement, 2015. **59**: p. 110-128.
7. Soe, K.T., Y.X. Zhang, and L.C. Zhang, *Material properties of a new hybrid fibre-reinforced engineered cementitious composite.* Construction and Building Materials, 2013. **43**: p. 399-407.
8. Wang, S. and V.C. Li. *Polyvinyl alcohol fiber reinforced engineered cementitious composites: material design and performances*. in *Proc., Int'l Workshop on HPFRCC Structural Applications, Hawaii*. 2005. Citeseer.
9. Li, V.C., *On Engineered Cementitious Composites (ECC): A Review of the Material and Its Applications.* Journal of Advanced Concrete Technology, 2003. **1**(3): p. 215-230.

10. Fischer, G. and V.C. Li, *Effect of fiber reinforcement on the response of structural members.* Engineering Fracture Mechanics, 2007. **74**(1–2): p. 258-272.

11. Han, B. and J. Ou, *Embedded piezoresistive cement-based stress/strain sensor.* Sensors and Actuators A: Physical, 2007. **138**(2): p. 294-298.

12. Nguyen, D.L., et al., *Comparative electromechanical damage-sensing behaviors of six strain-hardening steel fiber-reinforced cementitious composites under direct tension.* Composites Part B: Engineering, 2015. **69**: p. 159-168.

13. Li, M., et al., *Multifunctional carbon black engineered cementitious composites for the protection of critical infrastructure*, in *High Performance Fiber Reinforced Cement Composites 6*. 2012, Springer. p. 99-106.

14. Lin, V.W., et al. *Mechanical and electrical characterization of self-sensing carbon black ECC.* in *SPIE Smart Structures and Materials+ Nondestructive Evaluation and Health Monitoring*. 2011. International Society for Optics and Photonics.

15. Ranade, R., et al., *Influence of micro-cracking on the composite resistivity of Engineered Cementitious Composites.* Cement and Concrete Research, 2014. **58**: p. 1-12.

16. Kuo-Sheng, C., et al., *Electrode models for electric current computed tomography.* Biomedical Engineering, IEEE Transactions on, 1989. **36**(9): p. 918-924.

17. Karhunen, K., et al., *Electrical Resistance Tomography for Assessment of Cracks in Concrete.* ACI Materials Journal, 2010. **107**(5): p. 523-531.

18. Hou, T.-C. and J.P. Lynch, *Electrical Impedance Tomographic Methods for Sensing Strain Fields and Crack Damage in Cementitious Structures.* Journal of Intelligent Material Systems and Structures, 2009. **20**(11): p. 1363-1379.

19. Li, V.C., *Engineered Cementitious Composites (ECC) Material, Structural, and Durability Performance*, in *Concrete Construction Engineering Handbook*, N. E, Editor. 2008, CRC: Boca Ration.

20. Lan, S., T.-S. Lok, and L. Heng, *Composite structural panels subjected to explosive loading.* Construction and Building Materials, 2005. **19**(5): p. 387-395.

21. Li, V.C., S. Wang, and C. Wu, *Tensile strain-hardening behavior of polyvinyl alcohol engineered cementitious composite (PVA-ECC).* ACI materials Journal, 2001. **98**(6).

22. Kanda, T., Z. Lin, and V.C. Li, *Tensile stress-strain modeling of pseudostrain hardening cementitious composites.* Journal of Materials in Civil Engineering, 2000. **12**(2): p. 147-156.

23. Zhang, M., M. Sharif, and G. Lu, *Impact resistance of high-strength fibre-reinforced concrete.* Magazine of Concrete research, 2007. **59**(3): p. 199-210.

24. Ahmed, S. and M. Maalej, *Tensile strain hardening behaviour of hybrid steel-polyethylene fibre reinforced cementitious composites.* Construction and Building Materials, 2009. **23**(1): p. 96-106.

25. Maalej, M., S.T. Quek, and J. Zhang, *Behavior of hybrid-fiber engineered cementitious composites subjected to dynamic tensile loading and projectile impact.* Journal of Materials in Civil Engineering, 2005. **17**(2): p. 143-152.

26. Song, J., et al., *Effect of fiber volume content on electromechanical behavior of strain-hardening steel-fiber-reinforced cementitious composites.* Journal of Composite Materials, 2015: p. 0021998314568169.

27. Xie, P., P. Gu, and J.J. Beaudoin, *Electrical percolation phenomena in cement composites containing conductive fibres.* Journal of Materials Science, 1996. **31**(15): p. 4093-4097.

28. Ding, Y., et al., *Concrete with triphasic conductive materials for self-monitoring of cracking development subjected to flexure.* Composite Structures, 2016. **138**: p. 184-191.

29. Li, V.C., *Engineered cementitious composites-tailored composites through micromechanical modeling.* 1998.

30. Maalej, M. and V.C. Li, *Introduction of strain-hardening engineered cementitious composites in design of reinforced concrete flexural members for improved durability.* Structural Journal, 1995. **92**(2): p. 167-176.

31. Li, V.C. and C.K. Leung, *Steady-state and multiple cracking of short random fiber composites.* Journal of engineering mechanics, 1992. **118**(11): p. 2246-2264.

32. Li, V.C. and H.-C. Wu, *Conditions for pseudo strain-hardening in fiber reinforced brittle matrix composites.* Applied Mechanics Reviews, 1992. **45**(8): p. 390-398.

33. Yang, E.-H., et al., *Fiber-bridging constitutive law of engineered cementitious composites.* Journal of advanced concrete technology, 2008. **6**(1): p. 181-193.

34. Victor, C.L., *From micromechanics to structural engineering-The design of cementitious composites for civil engineering applications.* Structural Eng./Earthquake Eng, 1993. **10**(2): p. 37-48.

35. Lin, Z., T. Kanda, and V.C. Li, *On interface property characterization and performance of fiber reinforced cementitious composites.* RILEM J. Concrete Science and Engineering, 1999. **1**: p. 173-184.

36. Pan, Z., et al., *Study on mechanical properties of cost-effective polyvinyl alcohol engineered cementitious composites (PVA-ECC).* Construction and Building Materials, 2015. **78**: p. 397-404.

37. Marshall, D., B.N. Cox, and A.G. Evans, *The mechanics of matrix cracking in brittle-matrix fiber composites.* Acta metallurgica, 1985. **33**(11): p. 2013-2021.

38. Marshall, D. and B. Cox, *A J-integral method for calculating steady-state matrix cracking stresses in composites.* Mechanics of materials, 1988. **7**(2): p. 127-133.

39. Wang, S. and V.C. Li, *High-early-strength engineered cementitious composites.* ACI Materials journal, 2006. **103**(2): p. 97.

40. Whiting, D.A. and M.A. Nagi, *Electrical resistivity of concrete-a literature review.* R&D Serial, 2003(2457).

41. Saleem, M., et al., *Effect of moisture, chloride and sulphate contamination on the electrical resistivity of Portland cement concrete.* Construction and Building Materials, 1996. **10**(3): p. 209-214.

42. Wang, X., Y. Wang, and Z. Jin, *Electrical conductivity characterization and variation of carbon fiber reinforced cement composite.* Journal of materials science, 2002. **37**(1): p. 223-227.

43. Newlands, M.D., et al., *Sensitivity of electrode contact solutions and contact pressure in assessing electrical resistivity of concrete.* Materials and Structures, 2008. **41**(4): p. 621-632.

44. Spragg, R., et al., *Factors that influence electrical resistivity measurements in cementitious systems.* Transportation Research Record: Journal of the Transportation Research Board, 2013(2342): p. 90-98.

45. Hansson, I. and C. Hansson, *Electrical resistivity measurements of Portland cement based materials.* Cement and Concrete Research, 1983. **13**(5): p. 675-683.

46. McCarter, W. and R. Brousseau, *The AC response of hardened cement paste.* Cement and Concrete Research, 1990. **20**(6): p. 891-900.

47. McCarter, W., et al., *Two-point concrete resistivity measurements: interfacial phenomena at the electrode–concrete contact zone.* Measurement Science and Technology, 2015. **26**(8): p. 085007.

48. Hou, T.-C. and J.P. Lynch. *Conductivity-based strain monitoring and damage characterization of fiber reinforced cementitious structural components*. in *Smart Structures and Materials*. 2005. International Society for Optics and Photonics.

49. Hou, T.-C. and J.P. Lynch. *Monitoring strain in engineered cementitious composites using wireless sensors*. in *Proceedings of the International Conference on Fracture (ICF XI), Turin, Italy, March*. 2005.

50. Zhdanov, M.S. and G.V. Keller, *The geoelectrical methods in geophysical exploration*. Vol. 31. 1994: Elsevier Science Limited.

51. Holder, D.S., *Electrical impedance tomography: methods, history and applications*. 2004: CRC Press.

52. Barber, D., *A review of image reconstruction techniques for electrical impedance tomography.* Medical physics, 1989. **16**(2): p. 162-169.

53. Karhunen, K., et al., *Electrical resistance tomography imaging of concrete.* Cement and Concrete Research, 2010. **40**(1): p. 137-145.

54. Seppänen, A., et al., *Electrical resistance tomography imaging of concrete*. Concrete repair, rehabilitation and retrofitting II. Taylor & Francis Group, London, 2009.

55. Hallaji, M. and M. Pour-Ghaz, *A new sensing skin for qualitative damage detection in concrete elements: Rapid difference imaging with electrical resistance tomography*. NDT & E International, 2014. **68**: p. 13-21.

56. Hallaji, M., A. Seppänen, and M. Pour-Ghaz, *Electrical impedance tomography-based sensing skin for quantitative imaging of damage in concrete*. Smart Materials and Structures, 2014. **23**(8): p. 085001.

57. ASTM, C., *39, Standard test method for compressive strength of cylindrical concrete specimens.* ASTM International, 2001.

58. Cundall, P.A. *A computer model for simulating progressive large scale movements in blocky rock systems*. in *Proc. Symp. Rock Fracture (ISRM), Nancy*. 2013.

59. Sawamoto, Y., et al., *Analytical studies on local damage to reinforced concrete structures under impact loading by discrete element method.* Nuclear engineering and design, 1998. **179**(2): p. 157-177.

60. Hentz, S., L. Daudeville, and F.V. Donzé, *Identification and validation of a discrete element model for concrete*. Journal of engineering mechanics, 2004. **130**(6): p. 709-719.

61. Hentz, S., L. Daudeville, and F.-V. Donzé, *Discrete element modeling of a reinforced concrete structure.* Journal of the Mechanical Behavior of Materials, 2009. **19**(4): p. 249-258.

62. Lian, C.Q., Z.G. Yan, and S. Beecham, *Modelling pervious concrete under compression loading–a discrete element approach*. Vol. 168. 2011: Trans Tech Publ.

63. Lian, C., Y. Zhuge, and S. Beecham, *Numerical simulation of the mechanical behaviour of porous concrete.* Engineering Computations, 2011. **28**(8): p. 984-1002.

64. Khattak, M.J., *Micro-Mechanical Modeling of Portland Cement Concrete Mixture.* 328 Proceedings of ICCOEE2012, Kuala Lumpur, Malaysia, June, 2012: p. 11-14.

65. Wang, S.-C., *Artificial neural network*, in *Interdisciplinary computing in java programming*. 2003, Springer. p. 81-100.

66. Griinke, T.J., *Development of an artificial neural network (ANN) for predicting tribological properties of kenaf fibre reinforced epoxy composites (KFRE).* 2013.

67. Shi, Z.-Q. and D. Chung, *Carbon fiber-reinforced concrete for traffic monitoring and weighing in motion.* Cement and Concrete Research, 1999. **29**(3): p. 435-439.

68. Zhang, Z. and K. Friedrich, *Artificial neural networks applied to polymer composites: a review.* Composites Science and technology, 2003. **63**(14): p. 2029-2044.

69. Oreta, A.W. and K. Kawashima, *Neural network modeling of confined compressive strength and strain of circular concrete columns.* Journal of Structural Engineering, 2003. **129**(4): p. 554-561.

70. Demir, F., *Prediction of elastic modulus of normal and high strength concrete by artificial neural networks.* Construction and Building Materials, 2008. **22**(7): p. 1428-1435.

71. Lee, S.-C., *Prediction of concrete strength using artificial neural networks.* Engineering Structures, 2003. **25**(7): p. 849-857.

72. Topcu, I.B. and M. Sarıdemir, *Prediction of properties of waste AAC aggregate concrete using artificial neural network.* Computational Materials Science, 2007. **41**(1): p. 117-125.

73. Nehdi, M., H. El Chabib, and M.H. El Naggar, *Predicting performance of self-compacting concrete mixtures using artificial neural networks.* ACI Materials Journal, 2001. **98**(5): p. 394-401.

74. Bilim, C., et al., *Predicting the compressive strength of ground granulated blast furnace slag concrete using artificial neural network.* Advances in Engineering Software, 2009. **40**(5): p. 334-340.

75. Lu, Y., et al., *Artificial neural network (ANN)-based crack identification in aluminum plates with Lamb wave signals.* Journal of Intelligent Material Systems and Structures, 2009. **20**(1): p. 39-49.

76. Staszewski, W., C. Boller, and G.R. Tomlinson, *Health monitoring of aerospace structures: smart sensor technologies and signal processing*. 2004: John Wiley & Sons.

77. Beale, M.H., M.T. Hagan, and H.B. Demuth, *Neural Network Toolbox™ getting started guide*. Matlab, Mathworks, R2012b, 2016.

78. Nielsen, M.A., *Neural networks and deep learning*. Vol. 25. 2015: Determination press USA.

79. Suh, M.-W., M.-B. Shim, and M.-Y. Kim, *Crack identification using hybrid neuro-genetic technique.* Journal of Sound and Vibration, 2000. **238**(4): p. 617-635.

80. Su, Z. and L. Ye, *Lamb wave propagation-based damage identification for quasi-isotropic cf/ep composite laminates using artificial neural algorithm: part i-methodology and database development.* Journal of intelligent material systems and structures, 2005. **16**(2): p. 97-111.

81. Wang, D., L. Ye, and Y. Lu, *A probabilistic diagnostic algorithm for identification of multiple notches using digital damage fingerprints (DDFs).* Journal of intelligent material systems and structures, 2009.

82. Su, Z., et al., *On selection of data fusion schemes for structural damage evaluation.* Structural Health Monitoring, 2009. **8**(3): p. 223-241.

83. Hay, T., et al., *A comparison of embedded sensor Lamb wave ultrasonic tomography approaches for material loss detection.* Smart Materials and Structures, 2006. **15**(4): p. 946.

84. Akkari, A., *Evaluation of a polyvinyl alcohol fiber reinforced engineered cementitious composite for a thin-bonded pavement overlay*. 2011, Minnesota Department of Transportation, Research Services Section.

85. Li, V.C. and T. Kanda, *Innovations forum: engineered cementitious composites for structural applications.* Journal of Materials in Civil Engineering, 1998. **10**(2): p. 66-69.

86. Torigoe, S.-i., et al., *Study on evaluation method for PVA fiber distribution in engineered cementitious composite.* Journal of Advanced Concrete Technology, 2003. **1**(3): p. 265-268.

87. Zhuge, Y., et al. *Material properties and impact resistance of a new lightweight engineered cementitious composite*. in *23rd Australasian Conference on*

Mechanics of Structures and Materials, (ACMSM23). 2014. Byron Bay, NSW, Australia. Southern Cross University, Lismore, NSW, Australia.

88. ASTM, C., *C78-09 (2009) Standard test method for flexural strength of concrete (using simple beam with third-point loading).* ASTM International, 2009.

89. Qian, S. and V.C. Li, *Simplified inverse method for determining the tensile strain capacity of strain hardening cementitious composites.* Journal of Advanced Concrete Technology, 2007. **5**(2): p. 235-246.

90. Shi, L., Y. Lu, and Y. Bai, *Mechanical and Electrical Characterisation of Steel Fiber and Carbon Black Engineered Cementitious Composites.* Procedia Engineering, 2017. **188**: p. 325-332.

91. Elkey, W. and E.J. Sellevold, *Electrical resistivity of concrete*. Norwegian Public Roads Administration Publication. 1995, 33 pp.

92. Hermes, P., et al. *Material Properties of a New Hybrid-Fiber Engineered Cementitious Composite*. in *Advanced Materials Research*. 2012. Trans Tech Publ.

List of Publications

Journal papers:

1. **Shi, L.**, Lu, Y., & Bai, Y. (2017). Mechanical and electrical characterisation of steel fiber and carbon black engineered cementitious composites. *Procedia Engineering*, *188*, 325-332.

2. **Shi, L.**, Lin, S. T. K., Lu, Y., Ye, L., & Zhang, Y. X. (2018). Artificial neural network based mechanical and electrical property prediction of engineered cementitious composites. *Construction and Building Materials*, *174*, 667-674.

3. **Shi, L.**, Lu, Y., & Bai, Y. Correlation of mechanical and electrical properties of steel fibre and carbon black engineered cementitious composites with cracking development. *Cement and Concrete Research* (submitted)

4. **Shi, L.**, Lu, Y. Crack detection in engineered cementitious composite using electrical resistivity tomography. (submitted)

5. **Shi, L.**, Lu, Y. Quantitative crack evaluation using electrical resistivity tomography for engineered cementitious composite in tensile test. (ready for submission)

Conference paper:

1. **Shi, L.F.**, Lin, T.K., Lu, Y. and Bai, Y. (2017). Property prediction of engineered cementitious composite using artificial neural network. In the Proceedings of the 4th International Conference on Smart Monitoring, Assessment and Rehabilitation of Civil Structures, 13-15, September, 2017, Zurich, Switzerland